JOURNAL OF GEOPHYSICAL RESEARCH: OCEANS, VOL. 118, 6914–6933, doi:10.1002/2013JC009071, 2013

Skill testing a three-dimensional global tide model to historical current meter records

Patrick G. Timko,[1,2,3] Brian K. Arbic,[2] James G. Richman,[4] Robert B. Scott,[5,6] E. Joseph Metzger,[4] and Alan J. Wallcraft[4]

Received 1 May 2013; revised 11 November 2013; accepted 17 November 2013; published 17 December 2013.

[1] We apply several skill tests to assess tidal currents within a three-dimensional, eddy resolving, global ocean circulation model compared to over 5000 observational velocity records spanning 40 years. We examine the skill of the HYbrid Coordinate Ocean Model (HYCOM) on a regional, basin, and global scale and in deep versus shallow water. On a global scale, we examine the model tidal kinetic energy (KE) compared to the tidal KE estimated from the observational velocity records. We examine the vertical structure of the model tidal KE by averaging over predetermined depth bins. We also investigate the ability of the model to satisfy the 95% confidence intervals of the individual tidal ellipse parameters. On a basin scale, we determine if any bias exists in model performance with regards to a particular part of the global ocean and further investigate if any variability of model skill exists within the ocean basins by testing the model against smaller subsets of the observations. Our results show that the skill of the nondata assimilative HYCOM is comparable to the skill of the altimetric-constrained model TPXO7.2. HYCOM is shown to have up to 20% higher skill in resolving the Greenwich phase of the tides on a global basis and demonstrates moderate skill in replicating the vertical structure of the tidal currents as represented by the current meters. HYCOM demonstrates up to 20% higher skill than TPXO7.2 for some ocean basins and some ocean regions but exhibits up to 20% weaker skill in the Southern Ocean.

Citation: Timko, P. G., B. K. Arbic, J. G. Richman, R. B. Scott, E. J. Metzger, and A. J. Wallcraft (2013), Skill testing a three-dimensional global tide model to historical current meter records, *J. Geophys. Res. Oceans*, *118*, 6914–6933, doi:10.1002/2013JC009071.

1. Introduction

[2] This paper presents skill tests of three-dimensional (3-D) tidal currents in a global ocean circulation model. In a previous work, *Timko et al*. [2012] compared tidal currents within HYbrid Coordinate Ocean Model (HYCOM) [*Chassignet et al*., 2007] to over 1800 current meter records in the North Atlantic basin. In this paper, we present a basin and global scale assessment of model skill. We examine model skill in both deep and shallow (less than 1000 m depth) water using regression analysis and we apply some of the skill tests presented in *Timko et al*. [2012]. Here, model skill is assessed by comparison to over 5000 observational velocity records distributed globally. The records include the 1800+ velocity records previously used by *Timko et al*. [2012]. However, for the sake of brevity the 1800+ velocity records used in the previous skill test of the North Atlantic Ocean have been regrouped into four larger regions here instead of the 12 regions presented in the original work.

[3] There is a growing literature on the improvements that arise in forward (nonassimilative) global barotropic tide models when parameterizations of internal wave breaking over rough topography are included [*Jayne and St. Laurent*, 2001; *Carrere and Lyard*, 2003; *Egbert et al*., 2004; *Arbic et al*., 2004; *Lyard et al*., 2006; *Uehara et al*., 2006; *Griffiths and Peltier*, 2008, 2009; *Green*, 2010]. The model-data validation in these papers focuses on sea surface elevations rather than on velocities (or kinetic energies). To our knowledge, no papers as yet have focused on comparisons of kinetic energies (either barotropic or baroclinic) in forward global tide models to kinetic energies found in current meter observations or data-assimilative models. These types of kinetic energy (KE); comparisons are part of the focus of our work here.

[1]Center for Ocean-Atmospheric Prediction Studies, Florida State University, Tallahassee, Florida, USA.
[2]Department of Earth and Environmental Sciences, University of Michigan, Ann Arbor, Michigan, USA.
[3]Centre for Applied Marine Sciences, Marine Science Laboratories, Bangor University, Menai Bridge, Anglesey, UK.
[4]Oceanography Division, Naval Research Laboratory, Stennis Space Center, Mississippi, USA.
[5]Institute for Geophysics, Jackson School of Geosciences, University of Texas at Austin, Austin, Texas, USA.
[6]Département de Physique and LPO, Université de Bretagne Occidentale, CNRS, Brest, France.

Corresponding author: P. G. Timko, Centre for Applied Marine Sciences, Marine Science Laboratories, Bangor University, Menai Bridge, Anglesey LL59 5AB, UK. (p.timko@bangor.ac.uk)

2169-9275/13/10.1002/2013JC009071

[4] Recent interest in tides has also motivated the development of global baroclinic (internal) tide models. Because global internal tide modeling is very expensive, it remains a new topic with relatively few published papers [*Arbic et al*., 2004; *Simmons et al*., 2004; *Hibiya et al*., 2006; *Simmons*, 2008; *Arbic et al*., 2010; *Müller et al*., 2012]. The *Arbic et al*. [2010] simulations utilize HYCOM, which is currently being developed by the United States Navy as an ocean forecast model. The HYCOM simulations employ both tidal and atmospheric forcing, in contrast to earlier baroclinic tide simulations that employed only tidal forcing. The presence of atmospheric forcing in HYCOM allows for a horizontally varying stratification, as in the actual ocean. *Arbic et al*. [2010] demonstrated that the sea surface signature of internal tides is impacted to first order by this horizontally varying stratification.

[5] Because HYCOM is being developed as an ocean forecast model with tides, there is continual interest in validating the model with observations including observations of tides. Typically, global tidal models have been compared to observations of sea surface elevation, taken from, for instance, the 102 pelagic tide gauges used by *Shum et al*. [1997], hydrodynamic barotropic tide models which assimilate satellite altimeter data [e.g., the TPXO7.2 model of *Egbert et al*., 1994], or direct altimetric measurements of both barotropic and baroclinic tidal sea surface elevation signals [*Ray and Mitchum*, 1996, 1997].

[6] Few studies comparing tidal currents in global numerical models versus observations can be found in the existing literature. *Luyten and Stommel* [1991] compared the M_2 tidal currents in a set of 315 deep-sea current observations to the data-assimilative numerical model of *Schwiderski* [1979]. *Ray* [2001] also compared currents estimated from assimilative barotropic tide models to those inferred from current meters. *Dushaw et al*. [1997] compared the barotropic tidal currents from the TPXO.2 model to the currents derived from acoustic tomography and to the current meters used by *Luyten and Stommel* [1991]. In the *Dushaw et al*. [1997] study both semidiurnal constituents M_2, S_2, K_2, and N_2 and diurnal constituents K_1, P_1, O_1, and Q_1 were included. The *Luyten and Stommel* [1991], *Dushaw et al*. [1997], and *Ray* [2001] studies all focussed on comparison of the barotropic tidal currents as opposed to the baroclinic tidal currents. Luyten and Stommel note in their study that "shallow records tended to be contaminated by baroclinic tidal currents [*Hendry*, 1977], and so all data from less than 1000 m depth were rejected." Dushaw et al. also note in their study that "baroclinic tidal currents do not affect the determination of the harmonic constants of the barotropic tidal currents [*Dushaw et al*., 1995] when reciprocal acoustic transmissions are used."

[7] HYCOM is a full 3-D model capable of representing the vertical structure of the ocean. Hence, we are able to compare the model output to current meters directly to determine if the model is able to capture the vertical structure of the baroclinic tidal currents. A test of global model skill of this type is not possible using barotropic models such as TPXO. Validation of a model with tides is a very important step toward being able to produce a 3-D view of tidal KE in the ocean. An accurate representation of tidal currents for the ocean will provide a better understanding of the energy available for mixing within the ocean interior.

[8] In section 2., we describe the model, model output, and observations used in this study as well as the skill tests used to assess model performance. For comparison to the model, the observations are grouped into major ocean basins as well as smaller geographic regions within the major ocean basins. In section 3., we apply regression analysis to assess model skill in representing the tidal KE on a global and basin scale. In section 4., we apply the skill tests, previously introduced by *Timko et al*. [2012], to determine if the semimajor axis of the model tidal currents lies within the 95% confidence intervals generated during the tidal harmonic analysis of the observations. These tests are applied at a global, basin, and regional scale to assess model skill. We also examine model skill on a regional level by assessing horizontal correlation between the model output and observations when grouped into depth bins. In section 5., we summarize our results.

2. Model, Observations, and Skill Tests

2.1. The HYCOM Simulation

[9] In this comparison, we use hourly output for the month of September 2004 from an eddy resolving simulation with embedded tides [*Arbic et al*., 2010, 2012; *Richman et al*., 2012; *Shriver et al*., 2012; *Timko et al*., 2012]. HYCOM was integrated with a horizontal equatorial resolution of 1/12.5° and 32 hybrid layers in the vertical direction. The 30 days of 1 hourly, whole domain 3-D model output used in this study requires approximately 8 terabytes storage space and represents a small sample of the full 6 year model simulation. Due to data storage constraints global 3-D model output at hourly intervals was produced only for the months of September 2004 and March 2009. A comparison of the March 2009 model output is not included in this paper. The tidal algorithm within HYCOM is still under development and the results presented here represent the current state of development.

[10] During execution, HYCOM spins up for 10 years with climatological forcing followed by 6 years of interannual forcing. Meteorological forcing was Fleet Numerical Meteorological and Oceanography Center (FNMOC) 3 hourly 0.5° Navy Operational Global Atmospheric Prediction System (NOGAPS) [*Rosmond et al*., 2002] with wind speeds scaled to be consistent with QuickSCAT observations. Additional details of global HYCOM simulations are described by *Metzger et al*. [2010].

[11] Tidal forcing is calculated using the astronomical tidal potential for the four largest semidiurnal constituents (M_2, S_2, N_2, K_2) and four largest diurnal constituents (K_1, O_1, P_1, Q_1). The potential is adjusted for the effects of solid earth body tides [*Hendershott*, 1972]. The effects of self-attraction and loading (SAL) [*Hendershott*, 1972; *Ray*, 1998] are estimated using a scalar approximation [*Ray*, 1998], with the scalar SAL coefficient $\beta = 0.06$, as described by *Arbic et al*. [2010]. We are aware that the use of a constant value for β is not ideal, however, the additional computational expense in calculating the spherical harmonics for the dynamic calculation of the SAL term would increase model execution time significantly and have not been implemented at the present time. *Arbic et al*. [2010] also describes the parameterized topographic wave drag scheme used in the HYCOM tide simulations. In HYCOM, the parameterized topographic wave drag

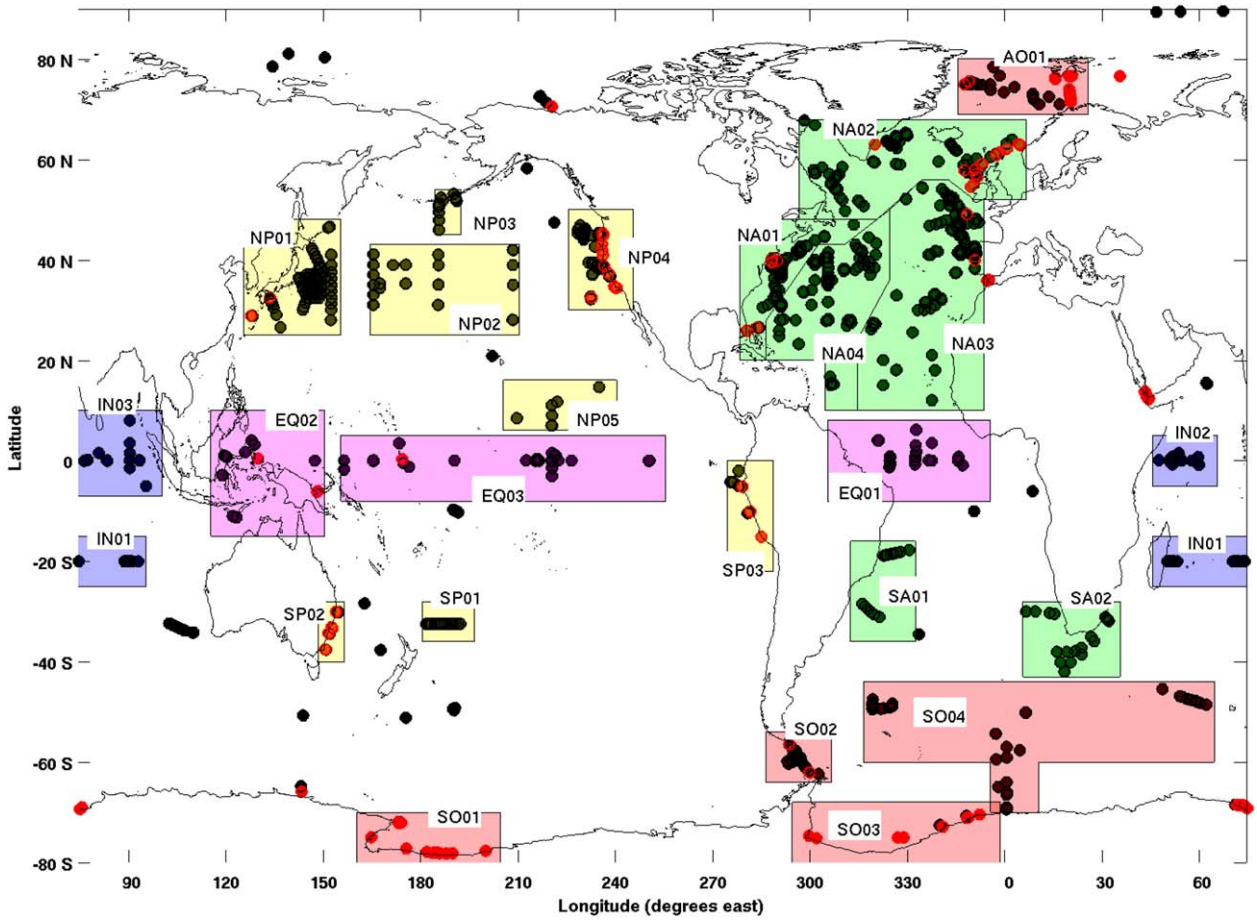

Figure 1. Mooring locations and regional groups used in the skill tests of HYCOM. Mooring locations depicted in red are in water less than 1000 m depth. See Table 2 for identification of the regions labeled within the figure.

represents the damping of tidal motions due to breaking internal gravity waves generated over rough topography. The strength of the globally averaged wave drag is tuned to minimize the RMS difference between tidal sea surface elevations in the model versus those recorded in 102 deep water tide gauges [*Shum et al*., 1997]. *Shriver et al*. [2012] presents the most recent improvements used in the wave drag scheme as well as a detailed comparison of the barotropic and baroclinic tidal sea surface height signals in HYCOM versus altimetric data.

2.2. The Current Meter Observations

[12] Velocity records chosen for comparison to the numerical model were identified from a current meter archive (CMA) of approximately 9000 unique time series previously used by *Scott et al*. [2010] and *Timko et al*. [2012]. The CMA spans ~40 years of observations. Some of the velocity records used in this study represents individual depth bins from ADCP's. The chosen velocity records satisfied the following criteria: (1) Time intervals between recorded values must not exceed 1 hour. (2) Records must contain a minimum of 105 days of observations. (3) Discontinuous records must provide a minimum of 105 days of data. A more detailed description of the criteria used for data selection, along with the sources for the observations contained within the CMA may be found in *Timko et al*. [2012] and *Scott et al*. [2010], respectively.

[13] Using the above criteria for selection we identified 5468 velocity records distributed over 1618 moorings. The mooring locations are not uniformly distributed across the world's major oceans. Figure 1 shows the distribution of moorings, and the 25 regional groups used in our skill tests. The 25 regions are grouped into 9 major ocean basins. For the purposes of this paper, we have defined the Southern Ocean as lying south of 45°S so that the Drake Passage and Antarctic Circumpolar Current both lie wholly within the Southern Ocean. The basin defined as the equatorial Atlantic ocean lies between 5°S and 5°N, bounded by South America to the west and Africa to the east. The equatorial Pacific is also defined between 5°S and 5°N and extends north and south throughout the western Pacific to include the Indonesian archipelago. Table 1 shows the number of velocity records and the number of moorings in each of the nine major ocean basins: North and South Atlantic, North and South Pacific, Indian Ocean, Arctic Ocean, and Southern Ocean as well as the equatorial Atlantic and equatorial Pacific, the latter including the Indonesian archipelago. The number of velocity records and moorings for the

Table 1. Number of Mooring Locations and Velocity Records (Instruments) for Each of the Nine Major Ocean Basins, and the Global Totals[a]

		Moorings	Instruments		Moorings	Instruments
Arctic (AO)	Total	90	296	Deep	37	163
	Sep	58	154	Shallow	53	133
N. Atlantic (NA)	Total	653	1882	Deep	588	1647
	Sep	395	972	Shallow	65	235
Eq. Atlantic (EQA)	Total	44	163	Deep	44	163
	Sep	8	20	Shallow	0	0
S. Atlantic (SA)	Total	38	119	Deep	38	119
	Sep	25	76	Shallow	0	0
N. Pacific (NP)	Total	345	1274	Deep	299	1135
	Sep	234	871	Shallow	46	139
Eq. Pacific (EQP)	Total	121	820	Deep	113	802
	Sep	73	457	Shallow	8	18
S. Pacific (SP)	Total	87	247	Deep	67	204
	Sep	34	94	Shallow	20	43
Indian Ocean (IN)	Total	102	303	Deep	82	199
	Sep	58	134	Shallow	20	104
South. Ocean (SO)	Total	138	364	Deep	91	240
	Sep	117	296	Shallow	47	124
Global	Total	1618	5468	Deep	1359	4672
	Sep	1002	3074	Shallow	259	796

[a]Shown are the total number, the number of records for the month of September, the number of records located in water depths greater than 1000 m (deep), and the number of records located in water depths less than 1000 m (shallow).

September, deep, and shallow water subsets for each of the nine ocean basins, and the totals for the global data set are also provided in Table 1. The distinction between the number of observations within the different subsets is made because some of the skill tests are applied separately to the subsets.

[14] Figure 2 illustrates the ability of HYCOM to match the vertical profile of velocity observations from a particular ADCP in the North Pacific. HYCOM matches very closely the semimajor axis and Greenwich phase of the M_2 tidal currents at this location. This is particularly true between 100 and 300 meters where the model values at both the model nearest neighbor and the best-fit neighbor lie within the 95% confidence intervals of the observed M_2 semimajor axis from the CMA. The model nearest neighbor is the model grid cell that lies closest to the mooring location. The best-fit neighbor is defined as the model grid cell within a 9 point neighborhood surrounding the mooring location (i.e., the model nearest neighbor and eight grid cells surrounding the nearest neighbor) which has the lowest RMS_{moor} score [*Timko et al*., 2012; see also equation (3) in this paper]. The 95% confidence intervals are determined by the Matlab routine t_tide [*Pawlowicz et al*., 2002] which is based upon the FORTRAN code of *Foreman* [2004] and which is used to analyze the model output. The match between HYCOM and the tidal analysis from the CMA is, in general, not as close as in the example shown in Figure 2. In general HYCOM is unable to represent bottom intensification due to the structure of the vertical coordinate. The vertical coordinate in HYCOM is represented by an isopycnal coordinate in deep water and may have a layer thickness of up to 500 m. In shelf regions, the vertical coordinate is a sigma coordinate but since the total number of layers decreases with decreasing depth the resolution of the bottom layers may not be sufficient to resolve the bottom boundary layers.

2.3. Tidal Kinetic Energy and Regression Analysis

[15] We present several measures for the difference in tidal KE between the model and observations. One measure is the mean KE ratio

$$\gamma = \frac{\sum_{i=1}^{M} \left[a_{\mathrm{mod}}^2 + b_{\mathrm{mod}}^2\right]_i}{\sum_{i=1}^{M} \left[a_{obs}^2(i) + b_{obs}^2(i)\right]}, \tag{1}$$

where i is an index of the instrument locations, M is the total number of instruments over which γ is computed, and the subscripts *mod* and *obs* denote model and observations, respectively, for the semimajor, a, and semiminor, b, axes. The indexing is written differently in the two cases to remind readers that HYCOM values are not exactly at the instrument locations but are taken from the model nearest neighbor.

[16] Another measure relating the modeled and observed tidal KE is the linear regression of the two, given by $KE_{mod} = A * KE_{obs}$. The regression coefficient A is the slope of the line that minimizes the square of the difference between the modeled and observed KE. The regression coefficient minimizes the square of the KE difference while the KE ratio relates the mean kinetic energies. Both measures are skewed toward the largest kinetic energies. Another measure, the relative bias D, used by *Scott et al*. [2010], defined by

$$D = \frac{\sum_{i=1}^{M} [a_{obs}^2(i) + b_{obs}^2(i)] - [a_{\mathrm{mod}}^2 + b_{\mathrm{mod}}^2]_i}{\sum_{i=1}^{M} [a_{obs}^2(i) + b_{obs}^2(i)] + [a_{\mathrm{mod}}^2 + b_{\mathrm{mod}}^2]_i}, \tag{2}$$

uses the difference in KE normalized by the sum of kinetic energies to reduce the impact of large kinetic energies. The relative bias can be calculated from the point-wise values of the normalized differences as well as from the global averages. The mean and median of the point-wise values do not

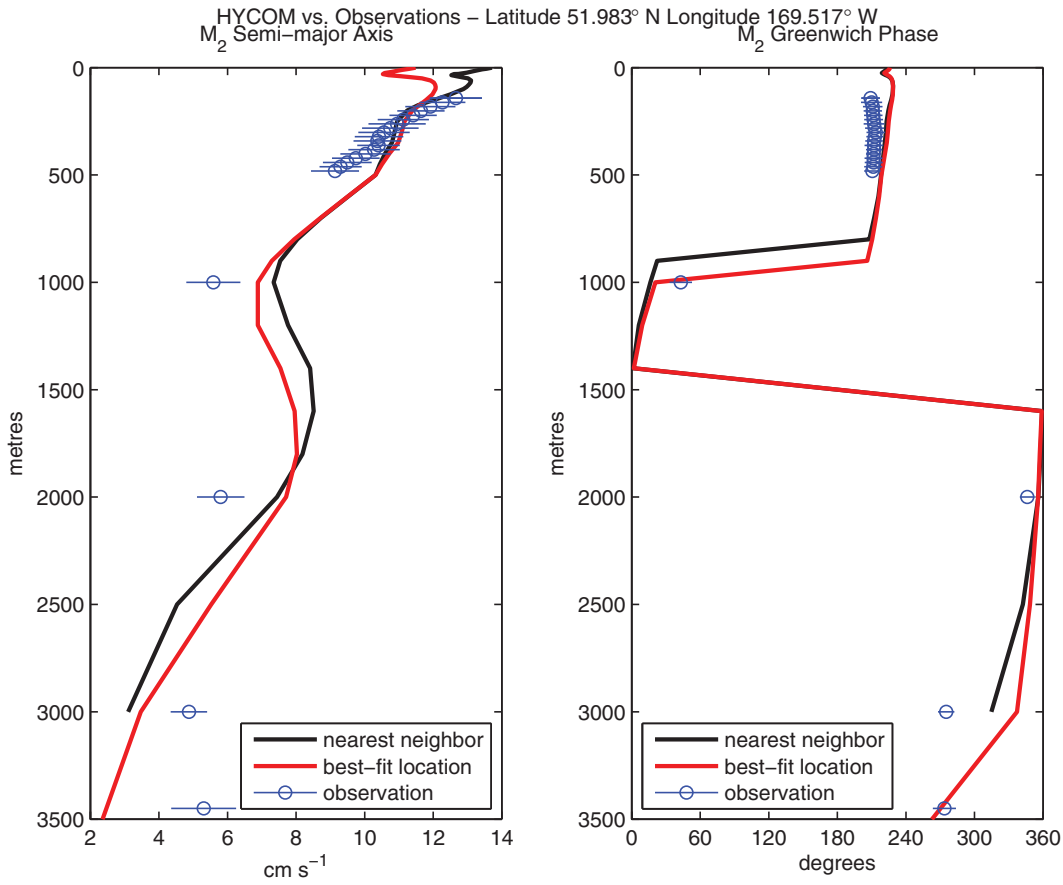

Figure 2. Comparison of M_2 semimajor axis and Greenwich phase in HYCOM and in a particular ADCP record as a function of depth. See plot title for ADCP location. The circles represent the value estimated from the observations and the line through the circle represents the 95% confidence intervals using harmonic tidal analysis. The black line shows HYCOM model values for the model grid point nearest the observation and the red line shows the model values for the best-fit neighbor from a 9 point block of grid cells surrounding the observation.

differ significantly from the global averages. The fourth measure used to examine the tidal KE is Pearson's correlation coefficient, R, between the model KE and observed KE.

[17] In section 3., we use regression analysis, summarized by values of γ, A, D, and R defined above, to discuss model performance in the global ocean and within major ocean basins. The results of the regression analysis provide an overall view of model performance. We also examine the differences that exist in model performance based upon water column depth. However, such an analysis does not provide information on the variability of model skill that may be present at a regional level within the larger basins.

2.4. Confidence Intervals, Root Mean Square Errors, and Spatial Correlations

[18] The global and basin scale regression analyses described above assess HYCOM skill using all of the available observations chosen from the CMA. We also estimate the skill of HYCOM by applying some of the skill tests first presented in *Timko et al.* [2012]. Consistent with the work of the aforementioned reference we examine HYCOM performance using a 9 point instrument neighborhood. Ideally, the model value at the nearest neighbor should provide the best model performance. However, since we only have 1 month of model output, differences between the stratification at the time of observation and model time as well as differences between model depth and true depth may affect the vertical modes and influence the baroclinic tidal structure. To account for this we expand our search to a 9 point neighborhood within the model to determine if any neighboring model values provide a better fit to the observations than the value at the nearest neighbor. As only 30 days of model output (from September 2004) are available for analysis we restrict our skill test using 95% confidence intervals to those observations that were taken in the month of September. This is done to avoid an inference problem that results due to the modulation of constituents S_2 and K_1 by constituents K_2 and P_1, respectively. Evaluation of model skill using 95% confidence intervals is applied at the global and basin scales. This analysis is presented in section 4.. The total number of instruments and moorings in each of the ocean basins is provided in Table 1.

[19] We also examine the variability that may exist within the nine major ocean basins. We extend our investigation of model skill using 95% confidence intervals by looking at 25 regional subsets within the September observations of the global data set (Figure 1 and Table 2). The 25 geographic regions are based upon the available data while providing a minimum of 10 moorings per region.

Table 2. Number of Moorings and Velocity Records (Instruments) for Each of the 25 Smaller Ocean Regions Shown in Figure 1 Along With a Brief Description of the Regional Sea or Current System Represented

Region	Moorings	Instruments	Description
AO 01	78	207	Greenland and Norwegian Seas
EQA01	44	163	Equatorial Atlantic
EQP01	22	137	Indonesian Archipelago
EQP02	99	683	Equatorial Pacific
IN 01	20	54	South Equatorial Current (Indian Ocean)
IN 02	30	64	Somali Current
IN 03	21	45	North Equatorial/Monsoon Current
NA 01	103	398	Gulf Stream
NA 02	197	484	High latitude North Atlantic
NA 03	183	485	Eastern North Atlantic
NA 04	159	401	Western North Atlantic
NP 01	126	400	Kuroshio/Oyashio Current
NP 02	36	111	North Pacific Current
NP 03	15	194	Alaska Current
NP 04	150	428	California Current
NP 05	14	49	North Equatorial Current
SA 01	14	36	Brazil Current
SA 02	19	62	Agulhas and Benguela Current
SO 01	28	97	Ross Sea
SO 02	39	83	Drake Passage
SO 03	15	30	Weddell Sea
SO 04	45	127	Antarctic Circumpolar Current
SP 01	19	49	East Auckland Current
SP 02	28	75	East Australian Current
SP 03	24	72	South Equatorial Current/Counter Current
GL 01	90	534	Global Ungrouped moorings
Global	1618	5468	

Note that some of the moorings shown in Figure 1 are isolated and do not lie within any of the 25 geographic regions shown in Figure 1. Velocity records at such locations were included in the global analysis but were not included in the basin scale or regional analyses.

[20] *Timko et al*. [2012] assessed the skill of HYCOM at matching the observed tidal velocities through the water column by applying a skill test based upon the root mean square error, RMS_{moor}, and correlation, CSS_{moor}, that existed between model and observed semimajor axis of the tidal ellipses on a single mooring. The CSS_{moor} statistic was found to be of limited usefulness since the large majority of the moorings available for comparison within the North Atlantic had only 3 or 4 velocity records and therefore required very high correlation to satisfy the 95% confidence level. The set of moorings used in this study also has the same problem (less than 25% of 1618 moorings having 5 or more velocity records) so we have not applied that skill test in this paper. However, in order to assess the best-fit neighbour in the skill tests presented here, we do compute RMS_{moor}, defined as

$$RMS_{moor}(n)=\sqrt{\frac{1}{m(n)}\sum_{k=1}^{k=m(n)}\left[A_{obs}(k)-A_{\mathrm{mod}}(k)\right]^2} \qquad (3)$$

where $\{A_{obs}(k)\}_{k=1}^{k=m(n)}$ are the m semimajor axis values estimated from the m instruments on a given mooring, n, and $\{A_{\mathrm{mod}}(k)\}_{k=1}^{k=m(n)}$ represents the corresponding model semimajor axis value for a given model neighbor. The best-fit location is determined using the observations from the appropriate subset of observations being tested. When we examine the ability of model values to lie within the 95% confidence intervals we only use the observations from the month of September. When we calculate the regional skill scores RMS_{reg} and CSS_{reg} defined below the best-fit location is calculated using the entire time series for the observations.

[21] In this paper, we assess the regional skill of HYCOM tidal currents within specified depth bins using the regional root mean square error, RMS_{reg}, and the regional correlation skill score, CSS_{reg} defined in *Timko et al*. [2012] as

$$RMS_{reg}=\sqrt{\frac{1}{I_{reg}(D)}\sum_{i=1}^{i=I_{reg}(D)}\left[a_{obs}(i)-a_{\mathrm{mod}}(i)\right]^2}, \qquad (4)$$

where the set $\{a_{obs}(i)\}_{i=1}^{i=I_{reg}(D)}$ represents the semimajor axis for $I_{reg}(D)$ instruments found within a specified depth bin $D=\{z_0\le z\le z_1\}$ for a predetermined ocean region and $\{a_{\mathrm{mod}}(i)\}_{i=1}^{i=I_{reg}(D)}$ are the corresponding model values; and

$$\frac{CSS_{reg}=\sum_{k=1}^{k=K}(x_k^{\mathrm{mod}}-\bar{x}^{\mathrm{mod}})(y_k^{obs}-\bar{y}^{obs})}{\sqrt{\sum_{k=1}^{k=K}(x_k^{\mathrm{mod}}-\bar{x}^{\mathrm{mod}})^2\sum_{k=1}^{k=K}(y_k^{obs}-\bar{y}^{obs})^2}}, \qquad (5)$$

is Spearman's rank correlation coefficient where $x_k^{\mathrm{mod}}, y_k^{obs}$ are the ranks of the sets $\{a_{\mathrm{mod}}(i)\}_{i=1}^{i=I_{reg}(D)}$ and $\{a_{obs}(i)\}_{i=1}^{i=I_{reg}(D)}$ (the sets defined over the same depth bins used to define RMS_{reg}), respectively, and $\bar{x}^{mod}, \bar{y}^{obs}$ are the means of the ranks. This analysis is done using all available data regardless of the time of year the observations were made. We also present the vertical profiles of the average RMS_{reg} and CSS_{reg} scores to provide some insight into how well HYCOM is able to represent the observed vertical structure of the tidal currents within a region. When examining the vertical profiles we restrict our attention to those regions in which five or more of the seven preselected depth bins contain at least three observations so that CSS_{reg} is defined through most if not all of the entire water column. The results of our analysis when testing model skill using 95% confidence intervals, RMS_{moor}, RMS_{reg}, and CSS_{reg} are presented in section 4..

3. Comparison to TPXO and Historical Current Meters

3.1. Barotropic Tidal Kinetic Energy on a Global Scale

[22] The regression analyses presented in this section give an overall view of the skill of 3-D (barotropic plus baroclinic) modeled tidal currents. To provide some context, we first provide an assessment of the skill of barotropic tidal KE. A comparison of the M_2 and K_1 barotropic KE per unit area in HYCOM versus TPXO7.2 is shown in Figure 3. The barotropic KE per unit area is given by $E=\rho_0 H(a^2+b^2)/4$, where $\rho_0=1035$ kg m^{-3} is average seawater density and H is the depth of the water column

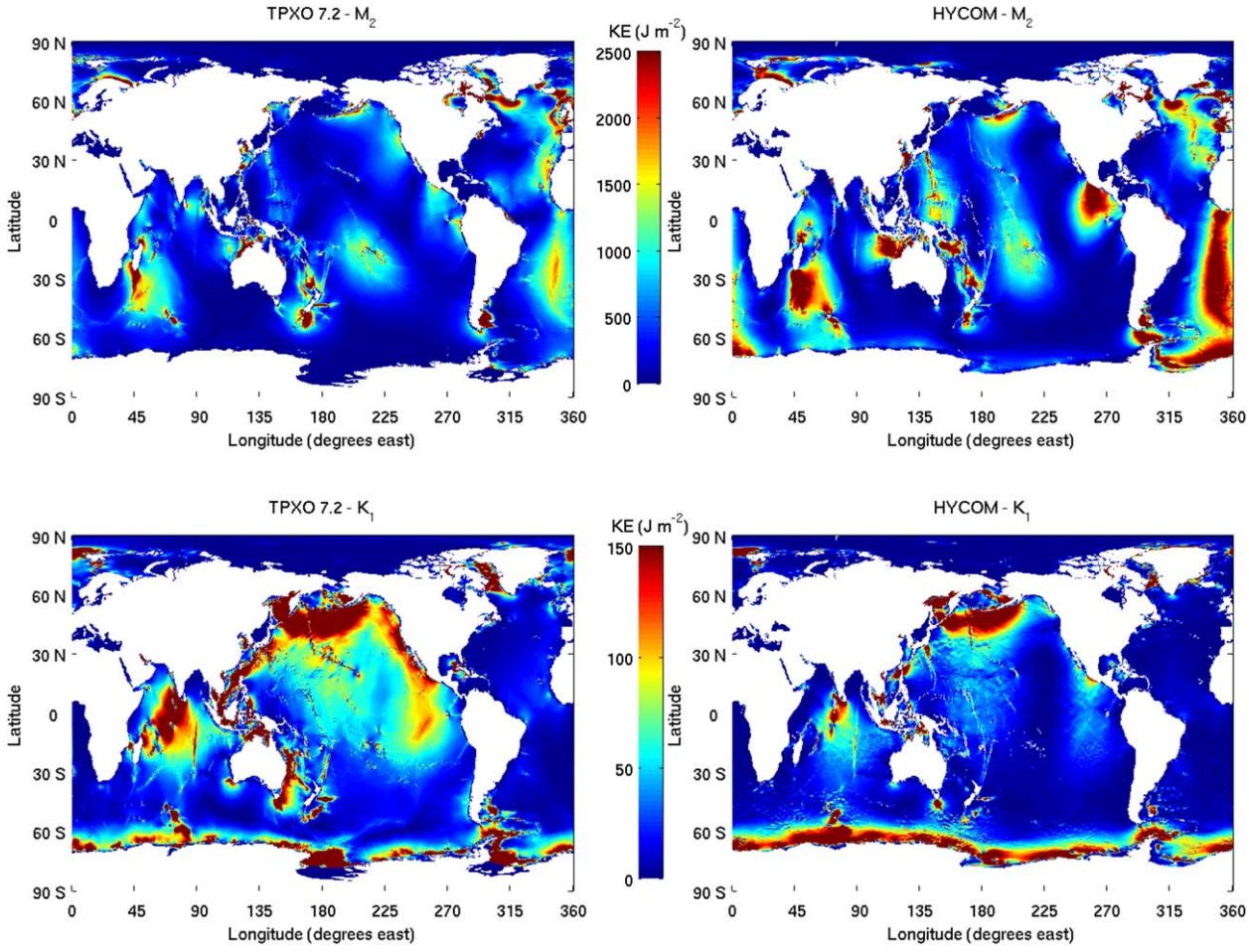

Figure 3. Global barotropic tidal kinetic energy per unit area (J m^{-2}) estimated from HYCOM and TPXO for constituents M_2 and K_1.

(*a* and *b* were defined earlier). TPXO7.2 provides global coverage on a uniform grid in contrast to the sparse spatial distribution of current meter data used elsewhere in this paper. The globally integrated barotropic KE of HYCOM and TPXO7.2 for constituents M_2, S_2, K_1, and O_1 is given in Table 3. Both Figure 3 and Table 3 indicate that the barotropic M_2 KE is higher in HYCOM ($100^{*}KE_{HYCOM}/KE_{TPXO} \sim 151\%$). While hotspots for KE are located in the same geographic regions in HYCOM and TPXO7.2 the barotropic M_2 KE in HYCOM tends to cover larger geographic regions and has a larger magnitude than TPXO7.2. HYCOM also exhibits a high level of barotropic M_2 KE in the Southern Ocean and South Atlantic between South America and Africa that is not observed in TPXO7.2. This is likely due to the inaccurate representation of bathymetry under floating ice shelves in HYCOM; at present HYCOM replaces floating ice shelves around Antarctica with land. *Timko et al*. [2012] noted weak HYCOM barotropic K_1 KE in the North Atlantic. It is clear from Figure 3 that the weakness in HYCOM barotropic K_1 KE ($100^{*}KE_{HYCOM}/KE_{TPXO} \sim 42\%$), reported in *Timko et al*. [2012], is global in extent. Weaker K_1 KE is observed in HYCOM along the west coast of North America, east coast of Asia, within the Indonesian archipelago, east coast of Australia and in the Indian Ocean. The globally integrated barotropic energy ratio ($100^{*}KE_{HYCOM}/KE_{TPXO}$) for constituent O_1 is 111% indicating a fairly good comparison. For constituent S_2 the ratio is 251% indicating that HYCOM is overly energetic. Some of the weak KE of K_1 and high KE of S_2 within HYCOM may be attributed to the modulation of constituents S_2 and K_1 by nearby constituents K_2 and P_1, respectively. The latter constituents exist in the model forcing but are not resolvable by harmonic analysis based upon the 30 days of model output available. *Timko et al*. [2012] were unable to find a consistent method by which to resolve the inference problem when analyzing the 30 days of HYCOM data available within the North Atlantic. We do not attempt to further address the inference issue here. Future simulations of HYCOM with embedded tides are expected to output several years of data at mooring locations to avoid this inference problem.

[23] In the following subsections, we describe the results of our regression analysis of tidal currents, in HYCOM versus current meters, on the global and basin scales. The model velocity values used in the comparison are interpolated to instrument depth at the model pressure grid point nearest to the geographic coordinates of the mooring location. Scatterplots of HYCOM tidal kinetic energies versus energies in current meter records are used to illustrate the distribution of HYCOM/observation pairs. Regression

Table 3. Globally Integrated Barotropic Tidal Kinetic Energy ($\times 10^{15}$ J) for HYCOM and TPXO

Constituent	HYCOM	TPXO	$100^{*}KE_{HYCOM}/KE_{TPXO}$
M_2	256.15	169.36	151.25
S_2	68.93	27.41	251.5
K_1	14.22	34.22	41.54
O_1	15.34	13.77	111.36

analysis summarizes overall trends. We also show a comparison of the kinetic energies averaged in vertical depth bins for those instruments located in water column depths exceeding 1000 m (deep water). The latter comparison reveals the skill of HYCOM in tracking the observed vertical structure of tidal KE.

3.2. Regression Analysis of 3-D Global Tidal Kinetic Energy

[24] Figure 4 shows scatterplots of the tidal KE in HYCOM versus current meters, for the four largest constituents. The KE for deep water (seafloor depth exceeding 1000 m) and shallow water (seafloor depth less than 1000 m) are shown separately. Aside from this separation by seafloor depth, no depth binning is performed in this figure. On each scatterplot, the one-to-one line is shown as a thick black line. Similar to the scatterplots of model versus CMA low-frequency KE shown in *Scott et al*. [2010], considerable scatter in the kinetic energies is observed, even with log-log plotting. It is clear from the shallow water plots that diurnal tides tend to be underestimated by the model. The suggestion is that HYCOM may underestimate the diurnal KE throughout the global domain, consistent with the results shown in Table 3. We are aware that some bias may exist due to the presence of signals for which the signal-to-noise ratio is small. This possible bias exists for both the semidiurnal and diurnal signals. It is not clear to us, however, that eliminating the weaker signals would not introduce a new bias by restricting the observations toward the surface where signals tend to be stronger.

[25] Values of γ computed over all deep water and all shallow water instruments are given in Table 4. The means of the kinetic energies used in the ratio are plotted as magenta squares in Figure 4. The mean KE is not located at the centroid of the cloud of kinetic energies plotted in the figures, reflecting the asymmetrical distribution of the kinetic energies around the mean which is skewed toward high KE levels.

[26] Comparison of γ for deep water and shallow water reveals that model skill is much greater in the open ocean than on the continental shelves and slopes. The KE ratio γ for the M_2 and S_2 constituents is higher than γ for the diurnal constituents. Constituent S_2 is found to be more energetic in the model than in the observations as in the comparison to TPXO7.2 as indicated in Table 3. In shallow water, the model K_1 and O_1 are very weak compared to observations while for the semidiurnal constituents $\gamma > 1$ in shallow water.

[27] The regression lines are plotted as bold red lines in Figure 4. The regression coefficients A, listed in Table 4, satisfy (approximately) $1/2 \leq A \leq 2/3$ in deep water, with the deep water S_2 value being the highest (0.71) and the

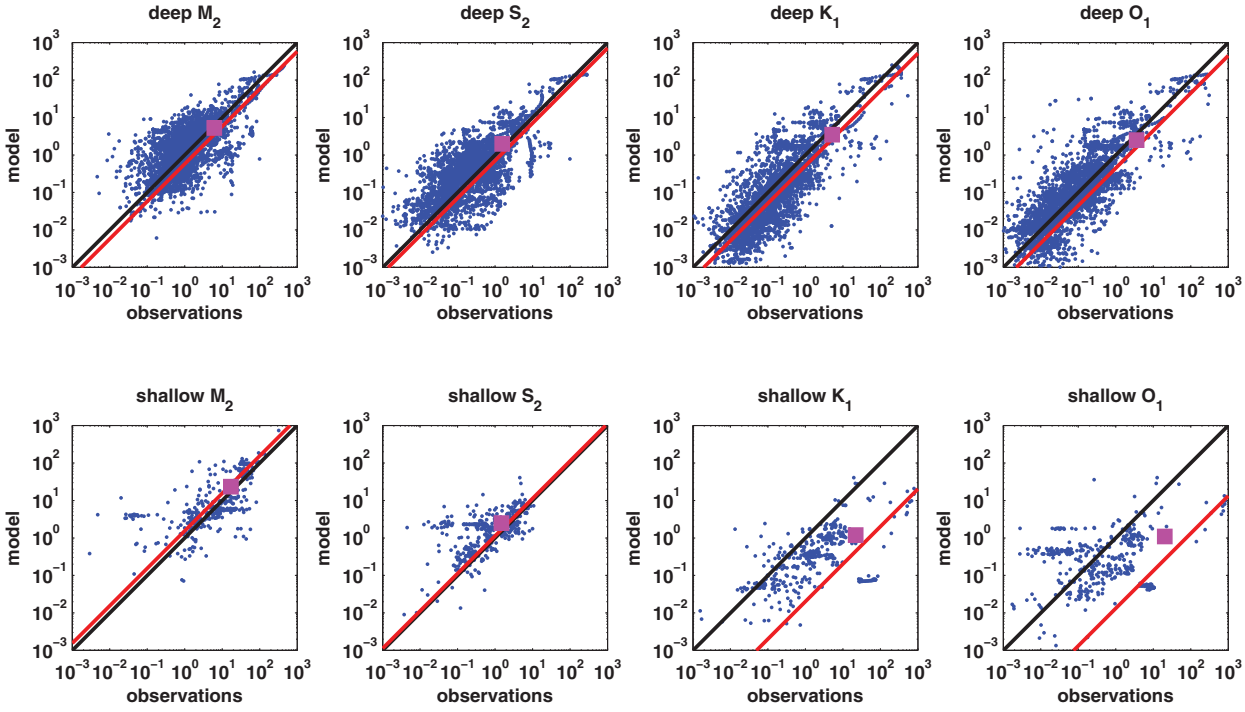

Figure 4. Log-Log scatterplot of the HYCOM tidal kinetic energy values ($cm^2\ s^{-2}$) versus the observed current meter values over the global ocean. The black line represents the one-to-one ratio. The red line represents the slope of the regression line. The magenta square represents the mean of the model values and observations.

Table 4. Values of the Kinetic Energy Ratio γ; Regression Coefficients A; Correlation Coefficients R; and Relative Bias D for HYCOM Tidal Kinetic Energy Comparisons With Current Meters[a]

	Deep				Shallow			
Constituent	γ	A	R	D	γ	A	R	D
M_2	0.85	0.58	0.86	0.08	1.37	1.56	0.85	−0.16
S_2	1.27	0.71	0.82	−0.12	1.68	1.12	0.56	−0.25
K_1	0.67	0.52	0.90	0.20	0.05	0.02	0.43	0.90
O_1	0.69	0.45	0.82	0.18	0.05	0.01	0.38	0.90

[a]See equations (1) and (2) and surrounding text for definitions of γ and D. "Shallow" denotes locations with seafloor depths less than 1000 m. "Deep"' denotes locations with seafloor depths greater than 1000 m. Values are computed for the four tidal constituents M_2, S_2, K_1, and O_1.

deep water diurnal values being the lowest (0.52 and 0.45 for K_1 and O_1, respectively). In shallow water, the semidiurnal regression values exceed one ($A \sim 1.12$–1.56) and are very small for the diurnal constituents ($A \sim 0.01$–0.02). The KE ratio γ and the regression coefficient A exhibit similar behaviors. Both measures indicate that the modeled (1) deep water semidiurnal kinetic energies lie within a factor of two (approximately) or better of the observed energies and (2) shallow water diurnal energies are very weak compared to those in observations. In both measures the modeled semidiurnal constituents perform better than diurnal constituents.

[28] The KE ratio γ and the regression coefficient A are measures of the gross energy levels of the model and the observations. The consistency of the spatial patterns of the energy levels can be assessed using the correlation coefficient, R. All constituents in both deep and shallow water have $0.4 \leq R \leq 0.9$ (Table 4). This indicates that the model has some skill in matching the spatial patterns of KE—i.e., the locations of strong and weak tidal currents—even though modeled diurnal KE is generally weak compared to the current meter energies.

[29] Table 4 also shows that there is small positive relative bias, D, for M_2 and small negative relative bias for S_2 in deep water indicating that model energies tend to be smaller than observations for M_2 and higher than observations for S_2. Larger positive relative bias $D \sim 0.2$ for the deep water diurnal tides indicate that the model underestimates the observed energy. In shallow water, model semidiurnal energies tend to be higher than observations while the very large relative bias $D \sim 0.9$ indicates that diurnal energies are much weaker than observed.

[30] All of the measures described here indicate that 32 layer HYCOM has some degree of skill in predicting the KE of tidal currents, even though the point-by-point agreement is often not close. The high correlation ($0.82 \leq R \leq 0.90$) between the modeled and observed KE in deep water suggests that the spatial distribution of the tidal energies is reproduced well. In shallow water only M_2 exhibits high correlation ($R = 0.85$) in the spatial distribution of KE. The other constituents only have weak to moderate correlation ($0.38 \leq R \leq 0.56$) with regards to the energy distribution in shallow water. With the notable exception of the diurnal K_1 and O_1 KE in shallow water, the globally averaged observed and modeled KE agree within a factor of 2 or better. The model performance is best for the deep water semidiurnal tides.

3.3. Vertical Structure of 3-D Tidal Kinetic Energy on a Global Scale

[31] An investigation of the vertical structure of the tidal KE should reveal the skill of the model in reproducing both barotropic and baroclinic tides. Seven depth bins are selected, with each depth bin containing at least 400 instruments. The average number of instruments in a depth bin is about 660, with the 2000–3000 m bin having the least (442) and the greater than 3000 m bin having the most (894). The vertical distribution of the tidal KE, averaged over deep water locations, is displayed in Figure 5. HYCOM performs best for M_2, with modeled and observed KE tracking each other well in the vertical. For S_2 HYCOM tracks the current meters reasonably well, though it tends to be more energetic as noted earlier in the HYCOM versus TPXO7.2 comparisons (Table 3). HYCOM is less successful for the diurnal constituents, particularly below 500 m where the modeled KE is much lower than the observed. Although the modeled diurnal energy is too low, the model does qualitatively reproduce the surface intensification of the diurnal energy. The curves in Figure 5 should not be considered as representative of the actual globally averaged vertical structure of the tidal KE, since the moorings are not distributed uniformly over the globe or in the vertical direction. Approximately 57% of the moorings are found in the Atlantic Ocean, where the diurnal barotropic tide is very weak. Approximately 59% of the moorings are found poleward of 35°, where the diurnal baroclinic tide cannot exist as a propagating wave. Thus, we expect the diurnal KE averaged over the current meter locations to be weak relative to the actual global average. However, the spatial distribution of the current meters does not explain why the modeled diurnal KE is too low. Finally, we note that only 15% of the moorings are found in the extratropical Southern Hemisphere.

[32] The vertical distributions of the relative measures introduced in the previous section—the KE ratio γ, A (regression coefficient), R (correlation coefficient), and D (relative bias)—are shown in Figure 6 and listed in Table 5. As in Figure 5, only deep water locations are included in this computation. Note that in Figure 6 we plot 1-D rather than D, so that the ideal value of all measures plotted is unity. The model performs best with M_2; the M_2 values of gamma γ, A, R, and 1-D all lie between 0.52 and 1.52, while the values for S_2 exhibit a wider range and the values for the diurnal constituents are often much lower indicating once again a weak bias in the model.

[33] The spatially averaged, semidiurnal M_2 and S_2 KE are within a factor of about two or better of those in the observations, over all depths. In fact, the agreement between HYCOM and current meters is generally better for semidiurnal tides than for the low-frequency flows examined in *Scott et al*. [2010]. However, HYCOM performance for diurnal tides is significantly worse; modeled diurnal tides are too weak.

3.4. 3-D Tidal Kinetic Energy on a Basin Scale

[34] We now discuss results on basin scales. Figure 7 shows scatterplots of the model versus observed M_2 KE for

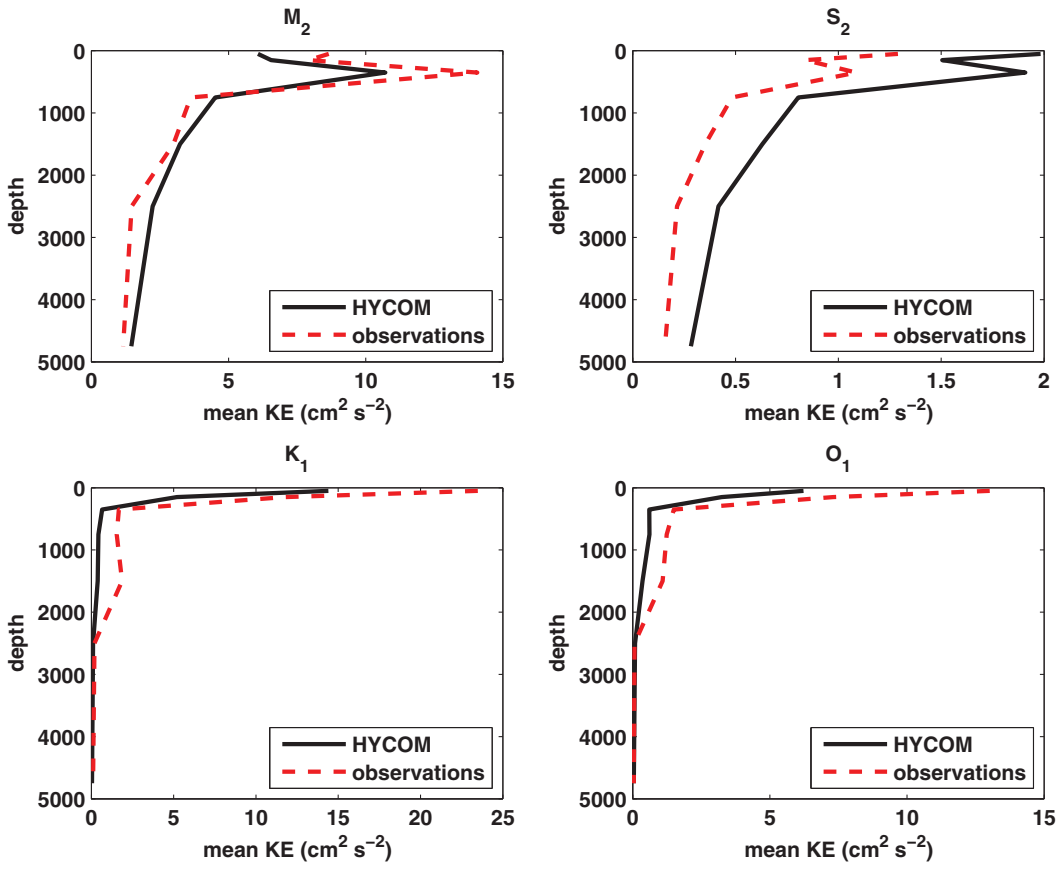

Figure 5. Vertical profiles of the average HYCOM and observed tidal kinetic energy averaged over seven depth bins for the global ocean in deep water (water column depth greater than 1000 m).

each of the major ocean basins. Figure 8 displays the same information but for K_1. Only values from deep water locations are included in the figures. As in Figure 4, the thick black lines represent the one-to-one correspondence, the red lines represent the regression A, and the magenta squares represent the mean KE of the model and observations used in the calculations of γ.

[35] For constituent M_2 (Figure 7), the amount of scatter appears to be fairly evenly distributed about the one-to-one ratio line in the Pacific Ocean (subplot NP, EQP, and SP) and also in the North Atlantic (subplot NA). The scatter tends to lie above the one-to-one line in all other ocean basins indicating that modeled M_2 KE in these regions tends to be higher than the observed M_2 KE. For constituent K_1 (Figure 8), the scatter tends to lie below the one-to-one ratio line for all ocean basins, consistent with earlier results, except in the North Pacific (subplot NP) and South Atlantic (subplot SA) where the scatter appears to be more uniformly distributed.

[36] Values for γ, A, R, and D for each ocean basin for the M_2 tidal constituent are provided in Table 6. The γ values in Table 6 indicate that the M_2 model KE is greater than the observed M_2 KE in all ocean basins except the North Atlantic and North Pacific where $\gamma = 0.93$ and $\gamma = 0.62$, respectively. Model KE is greater than the observed KE by a factor of two in the Southern Ocean and Equatorial Atlantic, and $1.2 \leq \gamma \leq 1.8$ in the Arctic Ocean, Equatorial and South Pacific Ocean, Indian Ocean, and South Atlantic Ocean. The regression coefficient, A, shown as a red line in Figure 7, satisfies $0.5 \leq A \leq 1.3$ with the North Pacific having the lowest value consistent with the low KE ratio γ for that ocean basin. Overall, $A < \gamma$, indicating that the total model KE, measured by γ, is biased toward locations where the model KE is very high compared to the observations. Correlation, R, is fair to very good with $0.50 \leq R \leq 0.94$ in all regions except the Equatorial Atlantic where it is very poor with $R = 0.11$. Only the North Atlantic basin appears to have little bias, $D = 0.03$. The North Pacific shows a positive bias (observed KE greater than model KE) with $D = 0.24$. For all other ocean basins, $-0.34 < D < -0.11$ indicating model KE is greater than observed KE.

[37] Table 6 also provides the γ, A, R, and D values for constituent K_1. The K_1 KE ratio, γ, is less than one in all ocean basins except the South Atlantic where $\gamma = 3.49$. Model K_1 KE is found to be very weak ($\gamma = 0.08$) compared to the observations in the Southern Ocean. In both the equatorial Atlantic and Pacific as well as in the South Pacific model K_1 KE is less than 1/2 the observed KE. In all other ocean basins, the model K_1 KE lies between 1/2 and 2/3 of the observed KE. The regression coefficient, A, shown as a red line in Figure 8, satisfies $A > 1/2$ only in the Indian Ocean, North Pacific, and South Atlantic.

[38] Correlation, R, for constituent K_1 varies from weak to very good across the different ocean basins. Correlation is weakest ($R = 0.04$) in the South Atlantic and is also

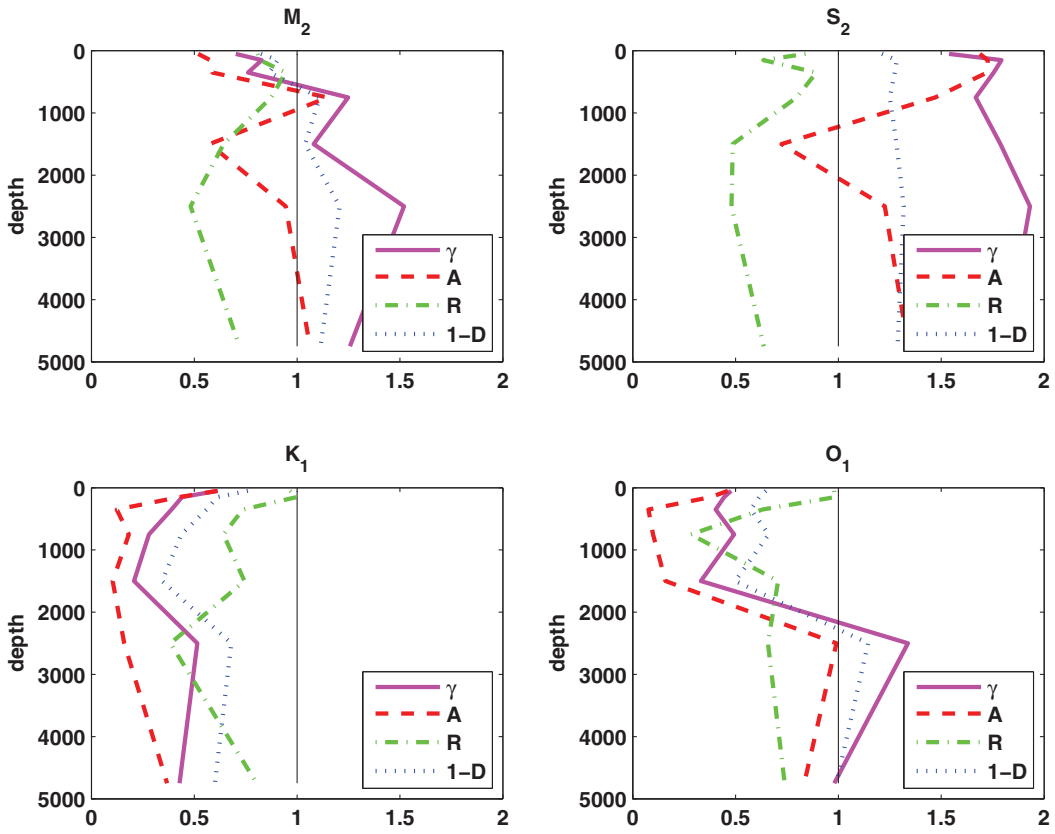

Figure 6. Vertical profile of the diagnostic quantities γ, A, R, and D (see text for definitions). Values are calculated over the global ocean for deep water (water column depth greater than 1000 m).

weak ($R = 0.17$) in the North Atlantic. Across the other ocean basins, $0.35 \leq R \leq 0.93$ with the highest correlation located in the North Pacific. All ocean basins except the South Atlantic have positive bias ($D > 0$) indicating that model KE is weak compared to observed KE. The greatest amount of bias is found to be in the Southern Ocean where $D = 0.85$; as noted earlier, we expect HYCOM to be inaccurate in the Southern Ocean due to the inadequate treatment of floating ice shelves. The least amount of bias is observed in the North Atlantic and Indian Ocean with $D = 0.19$ and $D = 0.20$, respectively.

Table 5. As in Table 4 but Sorted into Depth Bins and Only Using the Observations Located in Water Column Depth of 1000 m or More

Depth (m)	γ	A	R	1-D	γ	A	R	1-D
		M_2				S_2		
0–100	0.70	0.52	0.81	0.82	1.54	1.69	0.84	1.21
100–200	0.83	0.58	0.82	0.91	1.79	1.73	0.64	1.28
200–500	0.76	0.59	0.94	0.86	1.76	1.72	0.89	1.27
500–1000	1.25	1.15	0.87	1.11	1.67	1.47	0.80	1.25
1000–2000	1.08	0.57	0.64	1.04	1.79	0.72	0.49	1.28
2000–3000	1.52	0.94	0.48	1.21	1.93	1.23	0.48	1.32
3000–6500	1.26	1.06	0.72	1.11	1.81	1.34	0.64	1.29
		K_1				O_1		
0–100	0.61	0.61	0.97	0.76	0.48	0.46	0.98	0.65
100–200	0.44	0.43	1.00	0.61	0.44	0.38	0.98	0.62
200–500	0.39	0.12	0.74	0.56	0.40	0.08	0.63	0.57
500–1000	0.28	0.18	0.64	0.44	0.49	0.10	0.28	0.66
1000–2000	0.21	0.10	0.74	0.34	0.33	0.16	0.71	0.50
2000–3000	0.52	0.16	0.38	0.68	1.34	0.99	0.66	1.14
3000–6500	0.43	0.37	0.80	0.60	0.98	0.83	0.74	0.99

[39] The regression analysis within the individual basins indicates that HYCOM skill exhibits significant variability between different ocean basins and also between the M_2 and K_1 tidal constituents. HYCOM KE tends to be high compared to observations in all ocean basins except the North Atlantic and North Pacific for M_2 and tends to be low for K_1 except in the South Atlantic where it is much higher than the observed K_1 KE. Regression coefficients also indicate that M_2 generally performs much better than K_1. Differences between the KE ratio, γ, and the regression coefficient, A, indicate that the KE ratio tends to be dominated by a few high energy locations. Correlation scores are fair to very good in most ocean regions for both M_2 and K_1 suggesting that, even though the model KE tends to be high (low) for M_2 (K_1), HYCOM is able to describe the general horizontal distribution of KE. HYCOM also exhibits a bias in most ocean basins with model KE tending to be high for M_2 and low for K_1.

4. Testing Model Skill

[40] In this section, we test to determine if the parameters of the model tidal ellipses (semimajor axis, semiminor axis, inclination, and Greenwich phase) lie within the 95% confidence intervals generated by the Matlab routine t_tide [*Pawlowicz et al.*, 2002] from the analysis of the current meter records. We only use observations from the month of

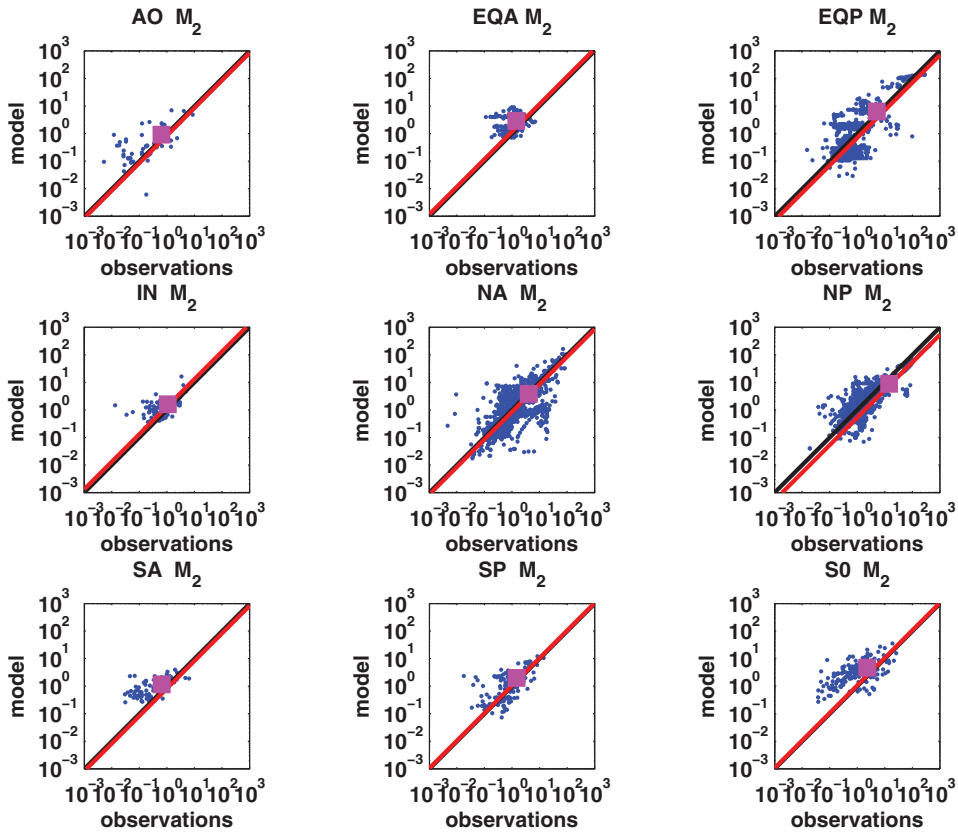

Figure 7. As in Figure 4 but for each of the ocean basins for constituent M_2 and only for locations of deep water (water column depth greater than 1000 m). See Table 1 for identification of the ocean basins for each subplot.

September. This test is conducted using the parameter values from the model nearest neighbor and also using all parameter values within the 9 point instrument neighborhood. In order to provide a baseline for comparison of the ability of the model velocity field to accurately simulate the barotropic tidal currents, we also test the ellipse parameter values from the HYCOM barotropic mode and the altimetric model TPXO7.2 at the nearest neighbor. Since HYCOM has a grid resolution of 1/12° and TPXO7.2 has a grid resolution of 1/4°, the comparison between the 3-D HYCOM velocity field using the best-fit from a 9 point neighborhood and the TPXO7.2 velocity at the model value nearest to the current meter latitude and longitude allows for a comparison over approximately the same geographic area. However, allowing a best-fit pick for HYCOM (as opposed to, for instance, an averaging over the neighborhood), obviously confers advantages for HYCOM in the comparison. We conduct our 95% confidence skill tests at the global, basin, and regional scales.

[41] At global and basin scales, this approach allows us to assess overall model skill as with the regression analysis presented in the previous section. On a regional scale, examination of model skill using 9 point instrument neighborhoods and 95% confidence intervals allows us to assess model skill at a local level to determine if any biases exist in the present model formulation.

[42] On the regional scale, we also examine the horizontal correlation between HYCOM and the observed tidal ellipse semimajor axis across the geographic regions shown in Figure 1. The instruments are grouped into predetermined depth bins across each region prior to calculating the correlation. Correlation is measured using both the model nearest neighbor and the best-fit neighbor for each instrument. When estimating the correlation the full observation records are used regardless of the time of year they were collected. Since many of the regions contain observations taken during different ocean observation programs our approach allows us to assess model performance against observations taken over several years and at different seasons.

4.1. 95% Confidence Intervals

[43] The 95% confidence interval skill test results for the four tidal ellipse parameters (semimajor axis, semiminor axis, inclination, and Greenwich phase) are shown in Figure 9. For both the HYCOM barotropic mode and TPXO7.2, and for all four major tidal constituents M_2, S_2, K_1, and O_1, between about 40–60% of the model values lie within the 95% confidence intervals of the observed semimajor axis. Both the M_2 and O_1 semimajor axis indicate ~10% less skill in HYCOM than TPXO7.2 at the nearest neighbor. For constituents S_2 and K_1 HYCOM has approximately the same skill as TPXO7.2. Within the 9 point instrument neighborhoods we see that HYCOM has between 5 and 10% higher skill than TPXO7.2 for constituents M_2, S_2, and K_1 and approximately equal to TPXO7.2 for constituent O_1.

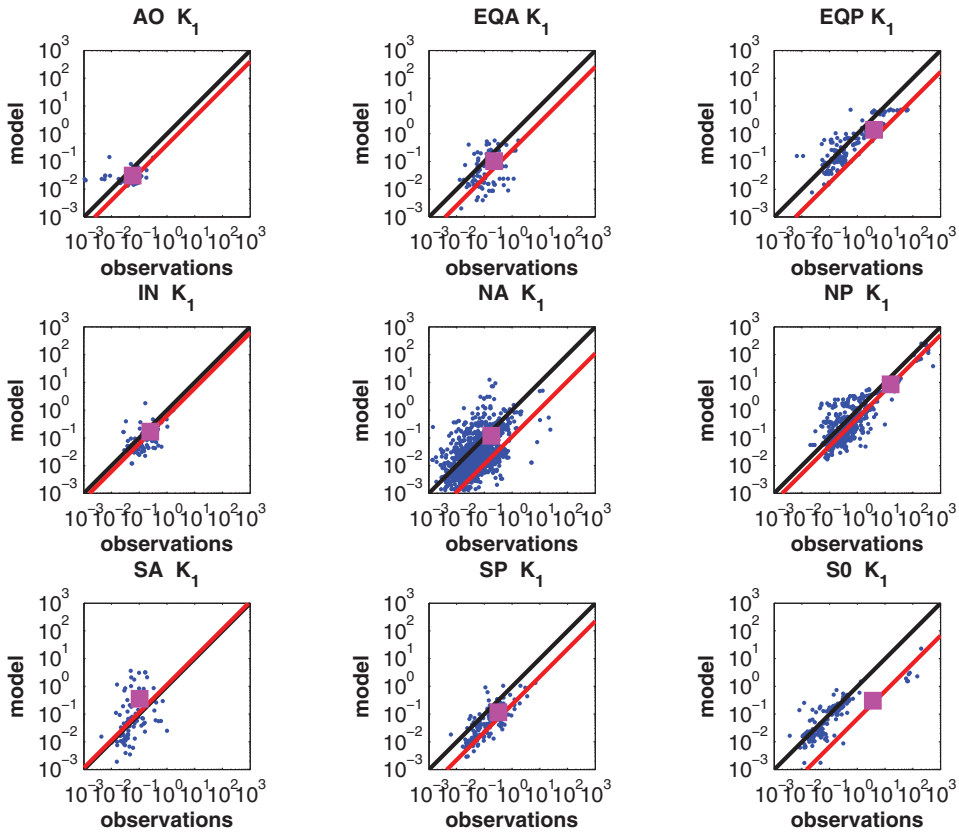

Figure 8. As in Figure 4 but for each of the ocean basins for constituent K_1 and only for locations of deep water (water column depth greater than 1000 m). See Table 1 for identification of the ocean basins for each subplot.

Table 6. As in Table 4 but for Each of the Major Ocean Basins and Only Using the Observations Located in Water Column Depth of 1000 m or More[a]

Basin	γ	A	R	D
		M_2 Deep Water		
AO	1.43	0.86	0.68	−0.18
EQA	1.99	1.18	0.11	−0.33
EQP	1.24	0.70	0.82	−0.11
IN	1.48	1.32	0.53	−0.19
NA	0.93	0.85	0.72	0.03
NP	0.62	0.53	0.94	0.24
SA	1.78	0.83	0.52	−0.28
SP	1.34	1.06	0.78	−0.15
S0	2.03	1.07	0.50	−0.34
		K_1 Deep Water		
AO	0.53	0.40	0.43	0.30
EQA	0.46	0.26	0.35	0.37
EQP	0.35	0.17	0.73	0.49
IN	0.67	0.61	0.65	0.20
NA	0.67	0.11	0.17	0.19
NP	0.53	0.50	0.93	0.30
SA	3.49	1.15	0.04	−0.55
SP	0.36	0.22	0.73	0.47
S0	0.08	0.07	0.82	0.85

[a]Only values for constituents M_2 and K_1 values are shown. See Table 1 for the definitions of the basins.

[44] The results for model semiminor axis and ellipse inclination are similar to those of the semimajor axis with the exception that the number of model values lying within the 95% confidence intervals of the observations ranges between 58 and 78% for the semiminor axis compared to 40–60% for the semimajor axis and ellipse inclination. At the nearest neighbour HYCOM performs less well than TPXO7.2. Within the 9 point instrument neighborhoods HYCOM has approximately the same amount of skill as TPXO7.2 for the semiminor axis of the tidal ellipses.

[45] The results of the skill test for Greenwich phase of the HYCOM velocity field shows 10–20% greater ability of the nearest neighbor to match the observed Greenwich phase than TPXO7.2, and 20–30% greater skill within the 9 point instrument neighborhoods. This suggests that HYCOM is able to model more accurately the timing of maximum currents through the water column than TPXO7.2. However, against this expectation we note that the HYCOM barotropic mode has 5–20% greater skill in predicting Greenwich phase than does either TPXO7.2 or even the 3-D model tidal currents evaluated at the nearest neighbor.

[46] We now compare model skill for the semimajor axis within each of the ocean basins. We restrict ourselves to the semi-major axis for the sake of brevity. Figure 10 shows the results of our analysis for the semimajor axis. For both TPXO7.2 and HYCOM skill is found to vary amongst the different ocean basins. For most ocean basins, the skill of TPXO7.2 is similar to the skill of the HYCOM barotropic

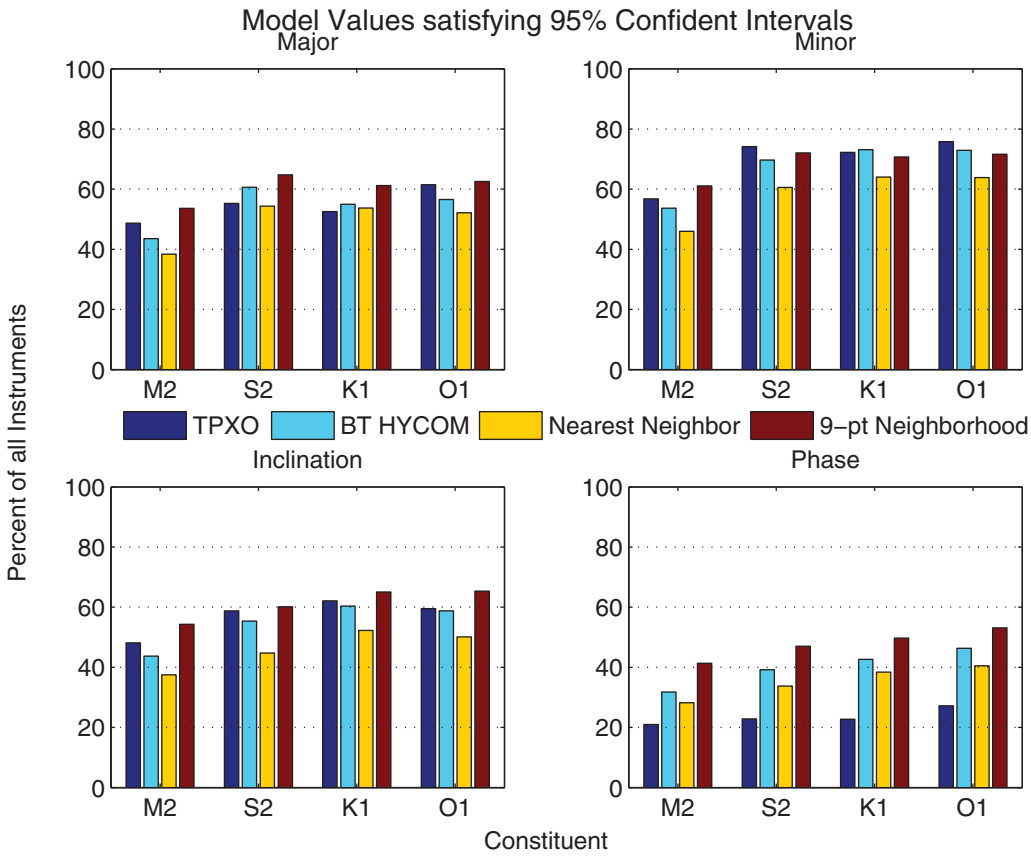

Figure 9. Number of model values from the global subset of September observations able to satisfy the 95% confidence intervals of the tidal ellipse parameters. "BT HYCOM" represents the barotropic mode of the model.

mode. Both TPXO7.2 and the HYCOM barotropic mode typically lie within the 95% confidence intervals of the observed semimajor axis between 40 and 60% of the time. Some notable differences between the skill of TPXO7.2 and the HYCOM barotropic mode do exist, however. In both the Arctic Ocean, representing the Norwegian and Greenland Seas, and the Southern Ocean TPXO7.2 has 25–35% greater skill than HYCOM for constituent O_1. In the equatorial Atlantic and South Pacific, the M_2 HYCOM barotropic mode has ~20% greater skill than TPXO7.2.

[47] The model semimajor axis estimated from the 3-D velocity field has up to 20% higher skill than TPXO7.2 in the equatorial Atlantic and Pacific, North and South Pacific for 11 out of 16 possible comparison pairs when tested at the model nearest neighbor. Within the 9 point instrument neighborhoods HYCOM has 0–40% greater skill than TPXO7.2 in 22 out of 36 comparisons. The greatest advantage of HYCOM is found in the equatorial Atlantic and the Pacific Ocean. In contrast, TPXO7.2 exhibits a clear advantage over HYCOM in the Southern Ocean.

[48] On a regional scale (Figure 11), HYCOM skill exhibits even greater variability than on a basin scale indicating that model performance varies locally and may be dependent on such factors as bathymetric representation and local stratification. The results of this analysis for the Arctic Ocean (AO01) and equatorial Atlantic (EQA(1)) are identical to the results presented in the basin scale analysis since these regions cover all of the instruments within the identified basins.

[49] In the Pacific Ocean, the skill of TPXO7.2 and the HYCOM barotropic mode differ by less than 20% for constituent M_2. For constituent K_1, TPXO7.2 exhibits 20% greater skill than the HYCOM barotropic mode in SP03. The HYCOM barotropic mode has 13–33% greater skill in the Indonesian Archipelago (EQP01), North Pacific Current System (NP02), Alaska Current System (NP03), and California Current System (NP05). All other differences for constituent K_1 are less than 10%. The skill of HYCOM does not increase significantly, and in some cases actually decreases, when the 3-D tidal currents are tested at the nearest neighbor. When tested within the 9 point neighborhoods HYCOM skill is 20–40% higher than TPXO7.2 for both M_2 and K_1 in the equatorial Pacific (EQP02), North Pacific Current sytem (NP02), Alaska Current System (NP03), and California Current System (NP05).

[50] In the Atlantic Ocean, TPXO7.2 exhibits up to 25% greater skill than HYCOM for the Gulf Stream system (NA01) and high latitude North Atlantic (NA02) even when the tidal currents are evaluated within the 9 point instrument neighborhoods. Differences in model skill between TPXO7.2 and HYCOM are less than 14% for the east and west North Atlantic regions (NA03 and NA04). A more detailed comparison and assessment of model skill in the North Atlantic may be found in *Timko et al*. [2012].

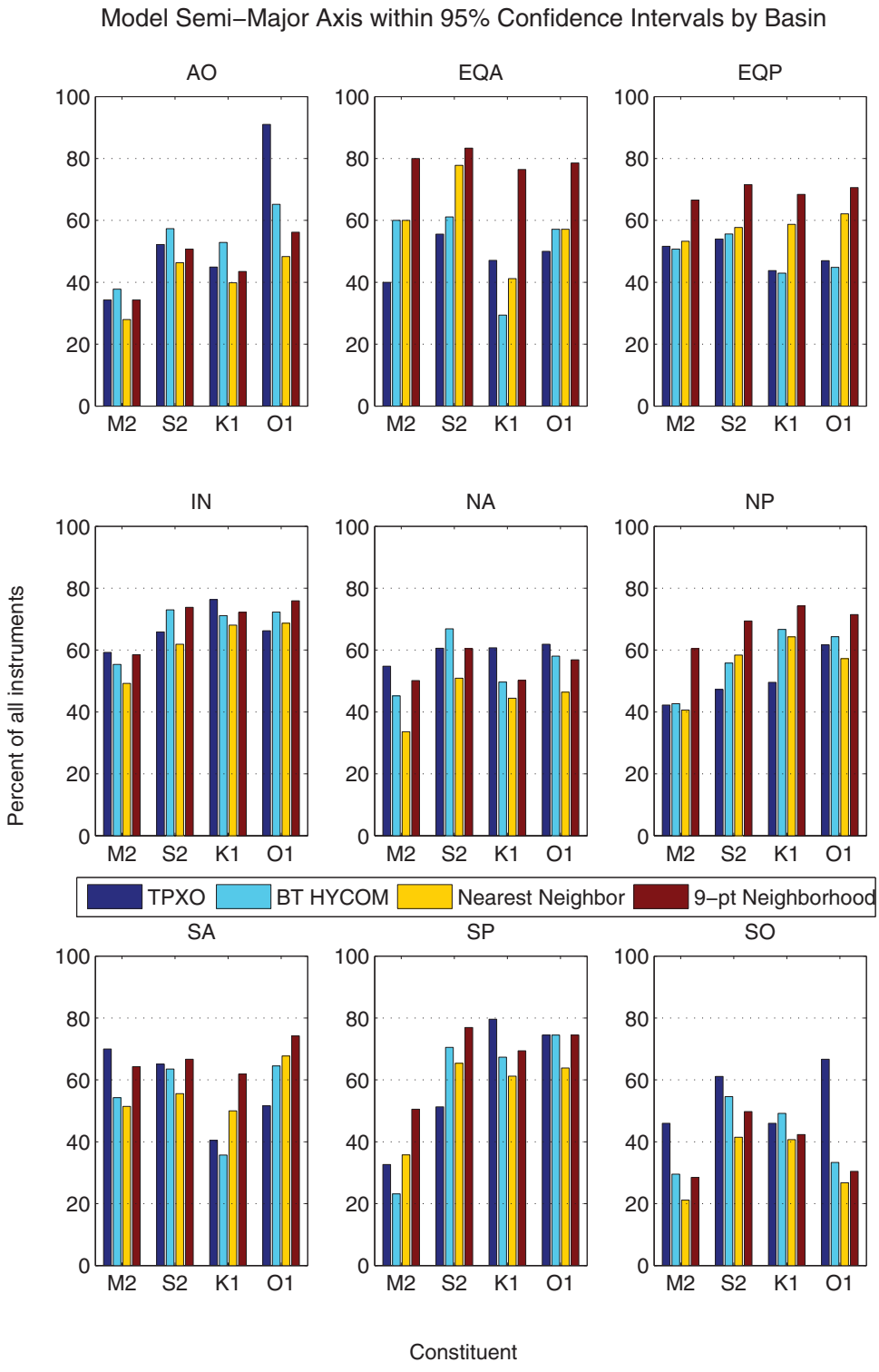

Figure 10. Same as Figure 9 but for each of the ocean basins and for the semimajor axis only. See Table 1 for identification of the ocean basins for each subplot.

[51] In the South Atlantic, TPXO7.2 has 46% greater skill than HYCOM for constituent M_2 in the Brazil Current system (SA01) while differences for constituent K_1 are less than 10%. In the Aghulhas and Benguela Current system, the K_1 tidal currents in HYCOM have 14% (28%) greater skill than TPXO7.2 at the nearest neighbour (within the 9 point instrument neighborhoods). For constituent M_2, the differences are less than 10%.

[52] In the Indian Ocean, TPXO7.2 has 10–15% greater skill than the HYCOM barotropic mode in the South Equatorial Current system (IN01) and up to 25% more skill than the 3-D currents. Differences in skill between TPXO7.2 and

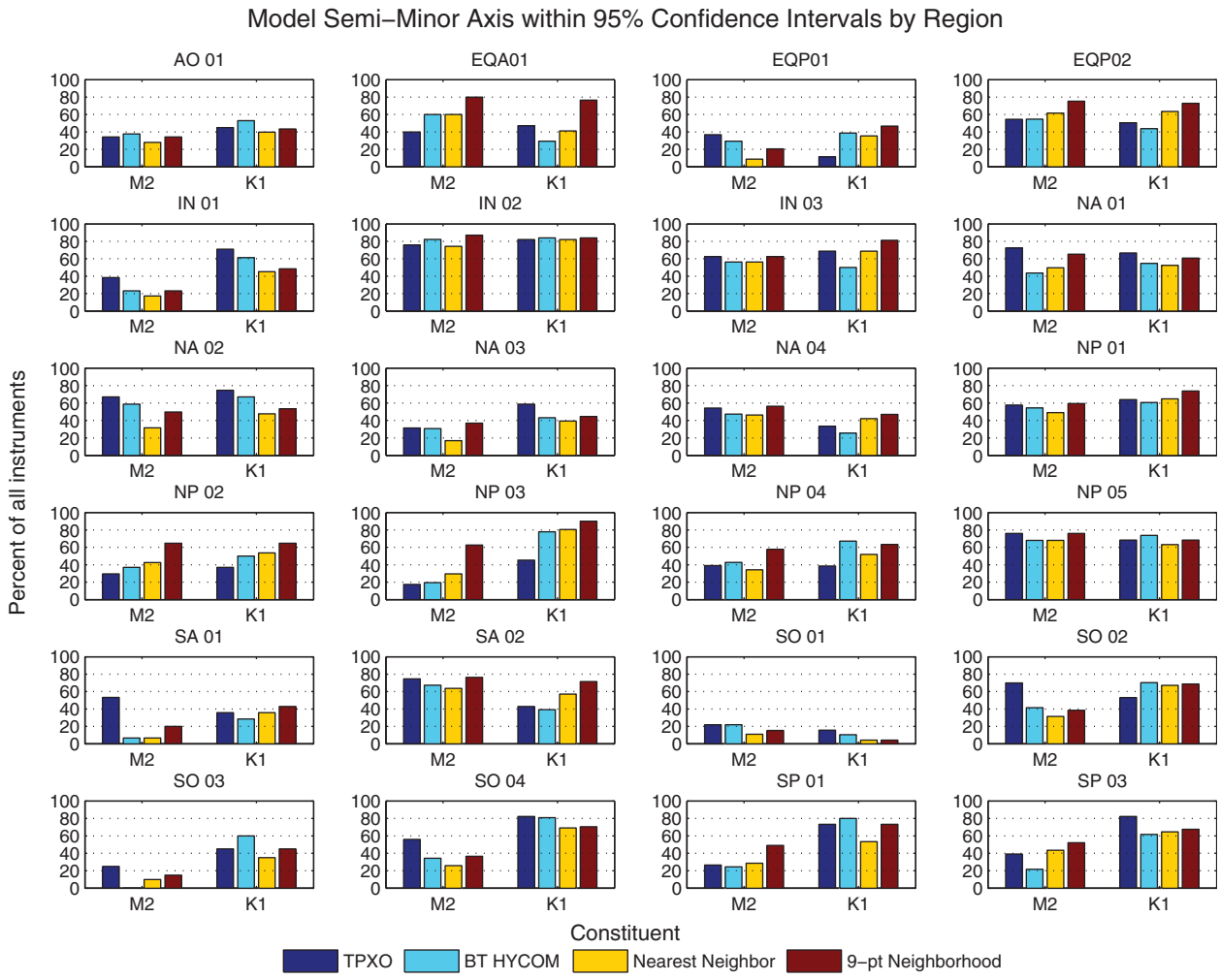

Figure 11. Same as Figure 9 but for each of the 25 individual ocean regions. Results are shown for the semimajor axis of constituents M_2 and K_1 only. No September data exists for SP02. See Table 2 for identification of the regions indicated in the individual subplots.

HYCOM are less than 20% in the Somali Current system (IN02) and North Equatorial/Monsoon Current system (IN03).

[53] In the Southern Ocean both models have less than 25% skill in the Ross Sea (SO01) and for constituent M_2 in the Weddell Sea (SO03). Differences in model skill for K_1 are less than 15%. TPXO7.2 has 30% greater skill than HYCOM for constituent M_2 in the Drake Passage (SO02) but exhibits 15–20% less skill than HYCOM for constituent K_1. In the Antarctic Circumpolar Current system (SO04), TPXO7.2 has 20–30% greater skill for constituent M_2 while differences for K_1 are less than 15%. Both models exhibit higher skill (70–80%) for K_1 than skill in representing M_2 (25–55%).

[54] Overall, the results from our analysis using 95% confidence intervals indicates that on a global scale the differences in model skill between TPXO7.2 and the HYCOM barotropic mode differ by less than 10% for the semimajor axis, semiminor axis, and inclination of the tidal ellipse. However, HYCOM exhibits 10–20% greater skill in predicting the phase of the tidal currents through the water column. For the 3-D velocity, HYCOM skill tends to be up to 20% less than TPXO7.2 when HYCOM is evaluated at the nearest neighbor but HYCOM skill improves by up to 20% when we search for the best-fit location within the 9 point neighborhoods. Our results also indicate that significantly variability in model skill exists for both HYCOM and TPXO7.2 on basin and regional scales.

4.2. Correlation

[55] Regional model skill may be evaluated using the RMS_{reg} and CSS_{reg} scores (equations (4) and (5)). The data are sorted into depth bins prior to calculation of the skill scores. Figure 12 shows those ocean regions for which significant correlations exist between the model and the observations of the M_2 semimajor axis between 200 and 500 m depth. The RMS_{reg} is represented by the thickness of the black boundary line outlining each region and CSS_{reg} is shown in color. The skill scores are calculated using the instrument nearest neighbor, CSS_{reg}(*nearest-neighbor*) (top) and also using the instrument best-fit neighbor, CSS_{reg}(*best-fit*) (bottom).

[56] CSS_{reg}(*nearest-neighbor*) was found to range from poor (no significant correlation) to very high (greater than 0.9) across the 25 regions we examined. CSS_{reg} was

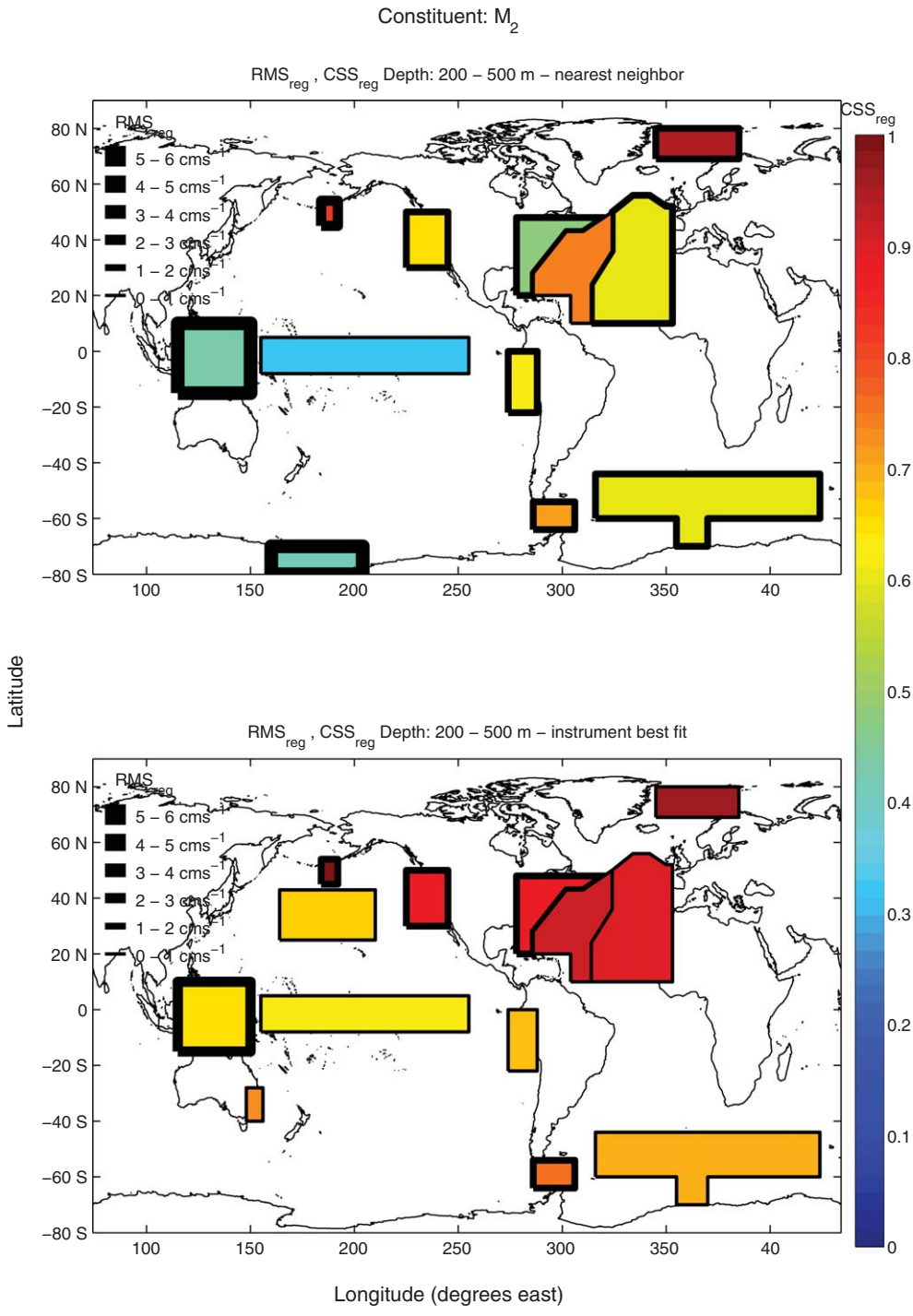

Figure 12. Horizontal correlation for M_2 semimajor axis at 200–500 m depth using the nearest neighbor (top) and best-fit location (bottom) for each of the ocean regions. The thickness of the black boundary outlining each region is the RMS_{reg}. Only those regions with significant correlations are shown. Significance is a one-sided test assuming correlation will be positive. See Figure 1 and Table 2 for identification of the individual regions depicted.

generally found to be higher in the northern hemisphere and lower in the southern hemisphere. In the southern ocean, the Drake Passage and ACC system have significant correlations between 0.5 and 0.7.

[57] When using the instrument best-fit locations CSS_{reg}(*best-fit*) generally increased for a region when compared to CSS_{reg}*(nearest-neighbor)* for that region. The exception to this is the Ross Sea where the CSS_{reg}*(best-fit)* value was found not to be significant even though CSS_{reg} (*nearest-neighbor*) was significant but weak. In contrast CSS_{reg}(*best-fit*) was found to be significant (0.6–0.7) in the North Pacific Current system and East Australian Current

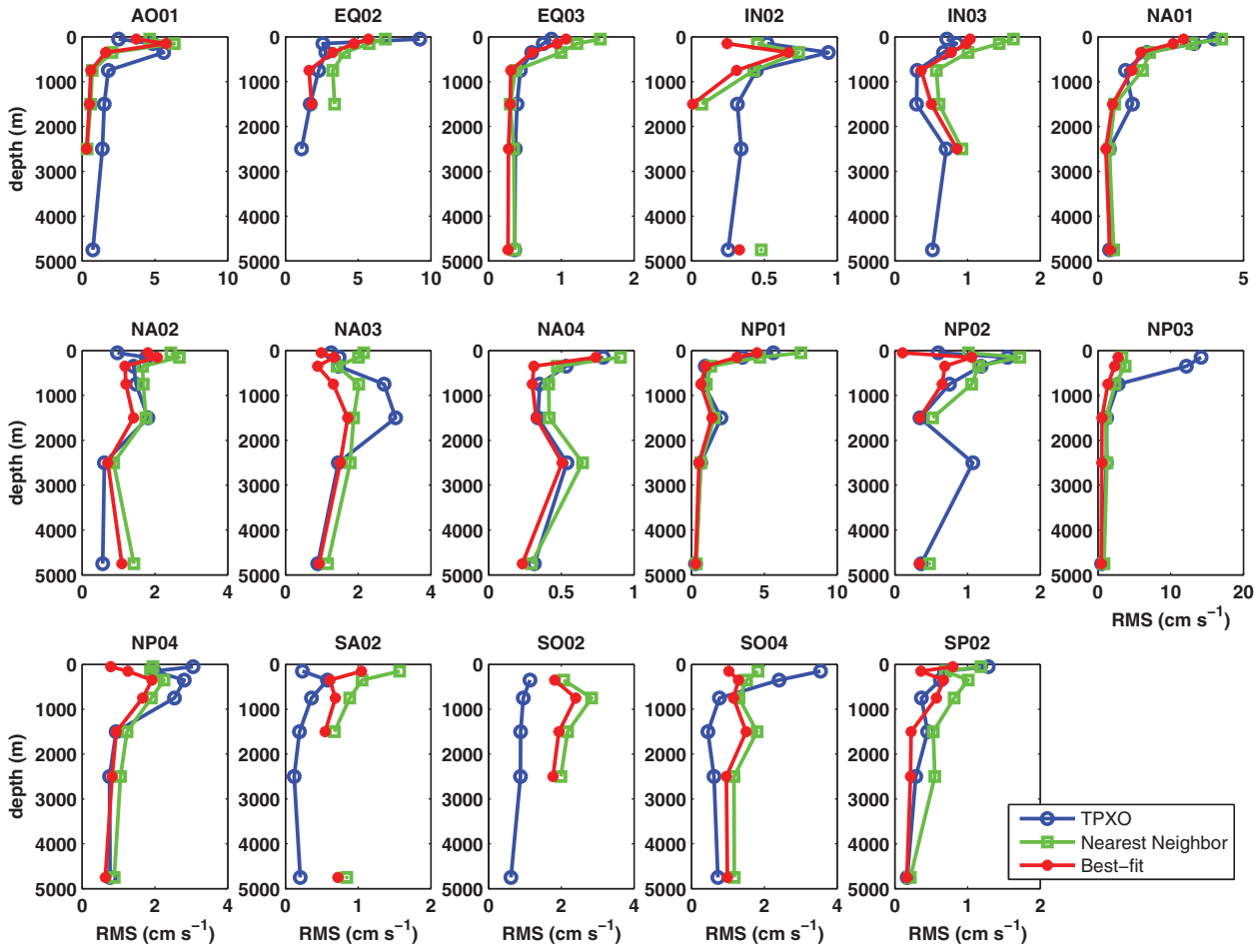

Figure 13. Vertical structure of the averaged RMS_{reg} values for TPXO, nearest neighbor, and best-fit locations. Only those regions with enough observations to represent the water column are shown. See Table 2 for identification of the individual subplots.

system even though CSS_{reg}*(nearest-neighbor)* was not. Generally, CSS_{reg}*(best-fit)* is very high (0.9) in the North Atlantic and high latitudes while in the midlatitude pacific and southern hemisphere CSS_{reg}*(best-fit)* it is lower (0.6–0.7).

[58] Vertical profiles of RMS_{reg}*(nearest-neighbor)*, RMS_{reg}*(best-fit)*, and RMS_{reg}*(TPXO)* for constituent M_2 are shown in Figure 13 for the 17 regions in which there were enough instruments in all of the seven depth bins to provide a meaningful representation of the water column. RMS_{reg}*(TPXO)* is calculated using the single model value for the semimajor axis, whereas RMS_{reg}*(nearest-neighbor)* and RMS_{reg}*(best-fit)* use HYCOM values estimated from the 3-D velocity field. From Figure 13, the RMS_{reg} values within each depth bin indicate that TPXO7.2 has more skill throughout the entire water column in the North Equatorial Current/Monsoon Current system, the Agulhas and Benquela Current systems, and in the Drake Passage (IN03, SA02, and SO02) when compared to RMS_{reg}*(best-fit)*. TPXO7.2 also exhibits greater skill in the top 200 m of the Arctic Ocean and high latitude North Atlantic (AO01 and NA02) and below 500 m depth in the Antarctic Circumpolar Current system (SO04). In contrast to this, we also observe that HYCOM has greater skill below 200 m depth in the Arctic Ocean (AO01); between 500 and 2000 m in the high latitude North Atlantic (NA02); in the top 2000 m of the eastern North Atlantic (NA03); in the top 1000 m of the North Pacific (NP02, NP03, and NP04); as well as the top 200 m of the Antarctic Circumpolar system (SO04). Other differences also exist but tend to show mixed results with either TPXO7.2 or HYCOM performing marginally better.

[59] The results of our regional correlation skill tests indicate that HYCOM is able to capture the horizontal variability of tidal currents for about 50% of the regions presented in this study. Correlations are low to high (0.3–0.9) at the nearest neighbor and moderate to very high (0.5–0.95) when the model is evaluated at the best-fit location. The vertical structure of the RMS_{reg} values indicates that HYCOM is able to capture some of the baroclinic structure in some regions. However, HYCOM is unable to capture the correct baroclinic structure in other regions.

5. Discussion

[60] We have presented the results of several skill tests to objectively evaluate the skill of tidal currents in a HYCOM simulation which is simultaneously forced by

atmospheric fields and the astronomical tidal potential. The skill tests compare tidal currents in HYCOM with an archive of 5468 current meter records spanning ~40 years.

[61] On a global scale, our results indicate that HYCOM barotropic tidal KE for the semidiurnal constituents M_2 and S_2 may be too high, while the diurnal constituent K_1 is too weak, when compared to TPXO7.2. Some of the energy mismatches for constituents S_2 and K_1 may be attributed to the modulation of these constituents by K_2 and P_1 which results from a tidal harmonic analysis based upon only 30 days of model output. We anticipate future HYCOM simulations will provide longer model time series for evaluation at current meter locations and will rectify this inference issue.

[62] Since HYCOM is a baroclinic model a comparison of tidal KE averaged across predetermined depth bins with that observed from the current meter records is also possible. We have employed four diagnostics (the KE ratio, regression coefficient, correlation coefficient, and relative bias) to further assess the skill of HYCOM in replicating the observed tidal structure through the water column. Spatially averaged KE for constituent M_2 appears to lie within a factor of two or less of observations throughout the water column and the relative bias for M_2 also tends to be small. For constituent S_2, HYCOM kinetic energies tend to be larger than observed and the relative bias also tends to be uniform throughout the water column. This result is consistent with our hypothesis that some of the low skill exhibited for constituent S_2 on a global scale may be the result of the modulation of S_2 by K_2 which produces a maximum for S_2 during the month of September.

[63] The inference problem associated with harmonic tidal analysis of only 30 days of model output may also partially explain why constituent K_1 model energies are much weaker than observations and the relative bias also tends to be large. For both S_2 and K_1 correlation coefficients vary from fair to good with very good correlation for K_1 in the top 200 m. Although the magnitudes of the HYCOM currents for S_2 and K_1 may not compare well with magnitudes in the observations (possibly due to the inference problem) the correlation scores indicate that HYCOM is able to capture some of the vertical structure of the S_2 and K_1 currents. Constituent O_1 also appears to be weak in the top 2000 m of HYCOM when compared to observations. Correlation also tends to be weak between 500 and 1000 m.

[64] When utilizing the 3074 observations taken in the month of September we find that the semimajor axis of the tidal ellipses estimated from the model output lie within the 95% confidence intervals of the observed semimajor axis between 40 and 60% of the time. The skill of HYCOM appears to be approximately equal to the skill ofTPXO7.2 in reproducing the observed semimajor/minor axis and ellipse inclination when the HYCOM grid is searched within a 1/4° box equal to the resolution of TPXO7.2. We have also presented evidence that HYCOM has 10–20% higher skill in reproducing the Greenwich phase of the observed tidal currents. The higher skill of HYCOM is not restricted to the 3-D velocity field but is also apparent in the HYCOM barotropic mode.

[65] On a basin scale, our skill tests indicate that the skill of HYCOM varies around the globe. HYCOM appears to have up to 20% greater skill than TPXO7.2 in the equatorial Atlantic and Pacific as well as in the North Pacific for some constituents. TPXO7.2, however, exhibits up to 40% greater skill in the Southern Ocean. At present, HYCOM replaces the floating ice shelves around Antarctica with land. This likely accounts for some of the low degree of skill of HYCOM in replicating the observed tides in the Southern Ocean. It is possible that this may also influence the barotropic tidal KE of HYCOM in the South Atlantic where significant differences exist between HYCOM and TPXO7.2.

[66] Application of our skill tests to smaller ocean regions demonstrates that HYCOM skill varies significantly within the larger ocean basins. This is most evident when we apply our skill test using 95% confidence intervals. HYCOM exhibits high skill compared to the current meter records in the equatorial Atlantic and Pacific oceans where up to 80% of the model semimajor axis values lie within the 95% confidence intervals within a 9 point neighborhood. Good model skill (greater than 60% of model semimajor axis values lying within the 95% confidence intervals) within 9 point neighborhoods is also exhibited by HYCOM in the Somali Current system, North Equatorial/Monsoon Current system, Kuroshio/Oyashio Current system, North Pacific Current system, Alaska Current system, California Current system, North Equatorial current system (within the North pacific), and Agulhas/Benguela Current system.

[67] The ability of HYCOM to represent the horizontal structure of tidal currents within specified depth bins has also been assessed. HYCOM has very good ($R > 0.9$) horizontal correlation with observations in the North Atlantic (excluding high latitudes), Norwegian and Greenland Seas, Alaska Current system, and California Current system. The model also exhibits good ($R > 0.6$) horizontal correlation in the North Pacific Current System, Indonesian Archipelago, Equatorial Pacific, East Australian Current System, Peru/Humbolt Current System, Drake Passage and Antarctic Circumpolar Current system.

[68] Our final skill test reveals the ability of HYCOM to model the vertical structure of the tidal currents when model values and observations are averaged over a geographic area. Our results show that in most of the ocean regions tested the RMS between HYCOM and observations are found to be smaller in the upper regions of the ocean than the RMS between TPXO7.2 and observations. The lower RMS scores for HYCOM indicate the ability of the HYCOM to provide a representation of the upper level tidal currents that is not possible with a barotropic model.

[69] In this paper, we have assessed the skill of HYCOM in replicating the tidal currents compared to an archive of current meter records spanning ~40 years. HYCOM is a baroclinic, eddy resolving ocean circulation model forced by both winds and tides. The algorithms for generating tidal forcing in HYCOM are still under development and the results presented here represent the ability of HYCOM to replicate tides at the present time. The skill tests presented, however, may easily be applied to other models and to smaller model domains in which tides play an important role in the circulation.

[70] **Acknowledgments.** We wish to thank those individuals who reviewed our manuscript and provided many useful comments which helped improve the presentation of this work. P.G.T. and B.K.A.

acknowledge support from a University of Texas Jackson School of Geosciences Development Grant, Naval Research Laboratory (NRL) contract N000173-06-2-C003, Office of Naval Research grants N00014-09-1–1003 and N00014-11-1–0487, and National Science Foundation grant OCE-0924481. R.B.S. acknowledges support from NSF grants OCE-0960834 and OCE-0851457, a contract with the National Oceanography Centre, Southampton, and a NASA subcontract to Boston University. This work was supported in part by a grant of computer time from the DOD High Performance Computing Modernization Program at the Navy DSRC. J.G.R., E.J.M., and A.J.W. acknowledge support from the Office of Naval Research (ONR) through the following project: ONR 6.2 Eddy Resolving Global Ocean Prediction Including Tides. This is contribution NRL/JA/7320-13-1674 and has been approved for public release. Distribution is unlimited. This is UTIG contribution 2597.

References

Arbic, B. K., S. T. Garner, R. W. Hallberg, and H. L. Simmons (2004), The accuracy of surface elevations in forward global barotropic and baroclinic tide models, *Deep Sea Res., Part II*, *51*, 3069–3101, doi:10.1016/j.dsr2.2004.09.014.

Arbic, B. K., A. J. Wallcraft, and E. J. Metzger (2010), Concurrent simulation of the eddying general circulation and tides in a global ocean model, *Ocean Modell.*, *32*, 175–187, doi:10.1016/j.ocemod.2010.01.007.

Arbic, B. K., J. G. Richman, J. F. Shriver, P. G. Timko, E. J. Metzger, and A. J. Wallcraft (2012), Global modelling of internal tides within an eddying ocean general circulation model, *Oceanography*, *25*, 20–29, doi:10.570/oceanog.2012.38 ''Special Issue on Internal Waves.''.

Carrere, L., and F. Lyard (2003), Modeling the barotropic response of the global ocean to atmospheric wind and pressure forcing—Comparisons with observations, *Geophys. Res. Lett.*, *30*, 1275, doi:10.1029/2002GL016473.

Chassignet, E. P., H. E. Hurlburt, O. M. Smedstad, G. R. Halliwell, P. J. Hogan, A. J. Wallcraft, R. Baraille, and R. Bleck (2007), The HYCOM (Hybrid Coordinate Ocean Model) data assimilative system, *J. Mar. Syst.*, *65*, 60–83.

Dushaw, B. D., B. D. Cornuelle, P. F. Worcester, B. M. Howe, and D. S. Luther (1995a), Barotropic and baroclinic tides in the central North Pacific Ocean determined from long-range reciprocal acoustic transmissions, *J. Phys. Oceanogr.*, *25*, 631–647.

Dushaw, B. D., G. D. Egbert, P. F. Worcester, B. D. Cornuelle, B. M. Howe, and K. Metzger (1997), A TOPEX/POSEIDEN global tidal model (TPXO.2) and barotropic tidal currents determined from long-range acoustic transmissions, *Prog. Oceanogr.*, *40*, 337–367.

Egbert, G. D., A. F. Bennett, and M. G. G. Foreman (1994), TOPEX/POSEIDON tides estimated using a global inverse model, *J. Geophys. Res.*, *99*, 24,821–24,852.

Egbert, G. D., R. D. Ray, and B. G. Bills (2004), Numerical modeling of the global semidiurnal tide in the present day and in the last glacial maximum, *J. Geophys. Res.*, *109*, C03003, doi:10.1029/2003JC001973.

Foreman, M. G. G. (2004), Manual for tidal currents analysis and prediction, *Pac. Mar. Sci. Rep. 78-6*, 65 pp., Inst. of Ocean Sci.

Green, J. A. M. (2010), Ocean tides and resonance, *Ocean Dyn.*, *60*, 1243–1253, doi:10.1007/s10236-010-0331-1.

Griffiths, S. D., and W. R. Peltier (2008), Megatides in the Arctic Ocean under glacial conditions, *Geophys. Res. Lett.*, *35*, L08605, doi:10.1029/2008GL033263.

Griffiths, S. D., and W. R. Peltier (2009), Modeling of polar ocean tides at the Last Glacial Maximum: Amplification, sensitivity, and climatological implications, *J. Clim.*, *22*, 2905–2924, doi:10.1175/2008JCLI2540.1.

Hendershott, M. C. (1972), The effects of solid earth deformation on global ocean tides, *Geophys. J. R. Astron. Soc.*, *29*, 389–402.

Hendry, R. M. (1977), Observations of the semidiurnal internal tide in the western North Atlantic Ocean, *Philos. Trans. R. Soc. London A*, *286*, 1–26, doi:10.1098/rsta.1977.0108.

Hibiya, T., M. Nagasawa, and Y. Niwa (2006), Global mapping of diapycnal diffusivity in the deep ocean based on the results of expendable current profiler (XCP) surveys, *Geophys. Res. Lett.*, *33*, L03611, doi:10.1029/2005GL025218.

Jayne, S. R., and L. C. St. Laurent (2001), Parameterizing tidal dissipation over rough topography, *Geophys. Res. Lett.*, *28*, 811–814.

Luyten, J. R., and H. M. Stommel (1991), Comparison of M_2 tidal currents observed by some deep moored current meters with those of the Schwiderski and Laplace models, *Deep Sea Res., Part A*, *38*, Suppl. 1, S573–S589.

Lyard, F., F. Lefevre, T. Letellier, and O. Francis (2006), Modelling the global ocean tides: Modern insights from FES2004, *Ocean Dyn.*, *56*, 394–415, doi:10.1007/s10236-006-0086-x.

Metzger, E. J., H. E. Hurlburt, X. Xu, J. F. Shriver, A. L. Gordon, J. Sprintall, R. D. Susanto, and H. M. van Aken (2010), Simulated and observed circulation in the Indonesian Seas: 1/12° global HYCOM and the INSTANT observations, *Dyn. Atmos. Oceans*, *50*, 275–300, doi:10.1016/j.dynatmoce.2010.04.002.

Müller, M., J. Y. Cherniawsky, M. G. G. Foreman, and J.-S. von Storch (2012), Global M_2 internal tide and its seasonal variability from high resolution ocean circulation and tide modelling, *Geophys. Res. Lett.*, *39*, L19607, doi:10.1029/2012GL053320.

Pawlowicz, R., B. Beardsley, and S. Lentz (2002), Classical tidal harmonic analysis including error estimates in MATLAB using T-TIDE, *Comput. Geosci.*, *28*, 929–937.

Ray, R. D. (1998), Ocean self-attraction and loading in numerical tidal models, *Mar. Geod.*, *21*, 181–192.

Ray, R. D. (2001), Inversion of oceanic tidal currents from measured elevations, *J. Mar. Syst.*, *28*, 1–18.

Ray, R. D., and G. T. Mitchum (1996), Surface manifestation of internal tides generated near Hawaii, *Geophys. Res. Lett.*, *23*, 2101–2104.

Ray, R. D., and G. T. Mitchum (1997), Surface manifestation of internal tides in the deep ocean: Observations from altimetry and tide gauges, *Prog. Oceanogr.*, *40*, 135–162.

Richman, J. G., B. K. Arbic, J. F. Shriver, E. J. Metzger, and A. J. Wallcraft (2012), Inferring dynamics from the wavenumber spectra of an eddying global ocean model with embedded tides, *J. Geophys. Res.*, *117*, C12012, doi:10.1029/2012JC008364.

Rosmond, T. E., J. Teixeira, M. Peng, T. F. Hogan, and R. Pauley (2002), Navy Operational Global Atmospheric Prediction System (NOGAPS): Forcing for ocean models, *Oceanography*, *15*, 99–108.

Schwiderski, E.W. (1979), Global Ocean Tides, Part II. The semidiurnal principal lunar tide (M_2). Atlas of Tidal Charts and Maps, *Technical Rep. TR 79–414*, 87 pp., Nav. Surface Weapons Cent., Dahlgren, Va.

Scott, R. B., B. K. Arbic, E. P. Chassignet, A. C. Coward, M. Maltrud, W. J. Merryfield, A. Srinivasan, and A. Varghese (2010), Total KE in four global eddying ocean circulation models and over 5000 current meter records, *Ocean Modell.*, *32*, 157–169, doi:10.1016/j.ocemod.2010.01.005.

Shriver, J. F., B. K. Arbic, J. G. Richman, R. D. Ray, E. J. Metzger, A. J. Wallcraft, and P. G. Timko (2012), An evaluation of the barotropic and internal tides in a high-resolution global ocean circulation model, *J. Geophys. Res.*, *117*, C10024, doi:10.1029/2012JC008170.

Shum, C. K., et al. (1997), Accuracy assessment of recent ocean tide models, *J. Geophys. Res.*, *102*, 25,173–25,194.

Simmons, H. L. (2008), Spectral modification and geographic redistribution of the semi-diurnal internal tide, *Ocean Modell.*, *21*, 126–138, doi:10.1016/j.ocemod.2008.01.002.

Simmons, H. L., R. W. Hallberg, and B. K. Arbic (2004), Internal wave generation in a global baroclinic tide model, *Deep Sea Res., Part II*, *51*, 3043–3068, doi:10.1016/j.dsr2.2004.09.015.

Timko, P. G., B. K. Arbic, J. G. Richman, R. B. Scott, E. J. Metzger, and A. J. Wallcraft (2012), Skill tests of three-dimensional tidal currents in a global ocean model: A look at the North Atlantic, *J. Geophys. Res.*, *117*, C08014, doi:10.1029/2011JC007617.

Uehara, K., J. D. Scourse, K. J. Horsburgh, K. Lambeck, and A. P. Purcell (2006), Tidal evolution of the northwest European shelf seas from the Last Glacial Maximum to the present, *J. Geophys. Res.*, *111*, C09025, doi:10.1029/2006JC003531.